



**DISSERTAÇÃO DE MESTRADO**

**FRETTING FATIGUE OF 6201 ALUMINUM ALLOY WIRES OF  
OVERHEAD CONDUCTORS: EXPERIMENTS AND LIFE  
PREDICTION**

**IAN DE MEDEIROS MATOS**

**Brasília, 06 de Março de 2020**

**UNIVERSIDADE DE BRASÍLIA**

FACULDADE DE TECNOLOGIA  
DEPARTAMENTO DE ENGENHARIA MECÂNICA

**UNIVERSIDADE DE BRASÍLIA  
FACULDADE DE TECNOLOGIA  
DEPARTAMENTO DE ENGENHARIA MECÂNICA**

**FRETTING FATIGUE OF 6201 ALUMINUM ALLOY  
WIRES OF OVERHEAD CONDUCTORS:  
EXPERIMENTS AND LIFE PREDICTION**

**IAN DE MEDEIROS MATOS**

**ORIENTADOR: FÁBIO COMES DE CASTRO**

**DISSERTAÇÃO DE MESTRADO EM CIÊNCIAS MECÂNICAS**

**PUBLICAÇÃO ENM.DM – XX/2020  
BRASÍLIA/DF: MARÇO – 2020.**



**UNIVERSIDADE DE BRASÍLIA  
FACULDADE DE TECNOLOGIA  
DEPARTAMENTO DE ENGENHARIA MECÂNICA**

**FRETTING FATIGUE OF 6201 ALUMINUM ALLOY  
WIRES OF OVERHEAD CONDUCTORS:  
EXPERIMENTS AND LIFE PREDICTION**

**IAN DE MEDEIROS MATOS**

DISSERTAÇÃO DE MESTRADO SUBMETIDA AO DEPARTAMENTO DE ENGENHARIA MECÂNICA DA FACULDADE DE TECNOLOGIA DA UNIVERSIDADE DE BRASÍLIA, COMO PARTE DOS REQUISITOS NECESSÁRIOS PARA A OBTENÇÃO DO GRAU DE MESTRE EM CIÊNCIAS MECÂNICAS.

APROVADA POR:

---

Prof. Fábio Comes de Castro, D.Sc. (ENM/UnB)  
(Orientador)

---

Prof. Jorge Luiz de Almeida Ferreira, D.Sc. (ENM/UnB)  
(Examinador interno)

---

Prof. Luis Augusto Mendes Veloso, D.Sc. (ENM/UnB)  
(Examinador externo)

**BRASÍLIA, 06 DE MARÇO DE 2020.**

## FICHA CATALOGRÁFICA

MATOS, IAN DE MEDEIROS

Fretting fatigue of 6201 aluminum alloy wires of overhead conductors: Experiments and life prediction.

[Distrito Federal] 2020.

xxi, 63p., 210 x 297 mm (ENM/FT/UnB, Mestre, Ciências Mecânicas, 2020)

Dissertação de Mestrado – Universidade de Brasília

Faculdade de Tecnologia.

Departamento de Engenharia Mecânica.

- |                       |                    |
|-----------------------|--------------------|
| 1. Overhead conductor | 2. Aluminum wire   |
| 3. Fretting fatigue   | 4. Life prediction |

## REFERÊNCIA BIBLIOGRÁFICA

MATOS, I. M., (2020) Fretting fatigue of 6201 aluminum alloy wires of overhead conductors: Experiments and life prediction. Dissertação de Mestrado em Ciências Mecânicas, Publicação ENM-DM xx/2020, Departamento de Engenharia Mecânica, Universidade de Brasília, Brasília, DF, 63p.

## CESSÃO DE DIREITOS

AUTOR: Ian de Medeiros Matos.

TÍTULO: Fretting fatigue of 6201 aluminum alloy wires of overhead conductors: Experiments and life prediction.

GRAU: Mestre ANO: 2020

É concedida à Universidade de Brasília permissão para reproduzir cópias desta dissertação de mestrado e para emprestar ou vender tais cópias somente para propósitos acadêmicos e científicos. O autor reserva outros direitos de publicação e nenhuma parte dessa dissertação de mestrado pode ser reproduzida sem autorização por escrito do autor.

---

Ian de Medeiros Matos  
SQS 109 Bloco D Apto 404  
70372-040 – Brasília - DF - Brasil  
[ian.m.matos@gmail.com](mailto:ian.m.matos@gmail.com)

# Agradecimentos

Aos meus pais, Kleuber e Simone, aos meus irmãos, Vitor e Gabriel, e à minha namorada, Carolina, que sempre acreditaram no meu sucesso e me deram todo carinho e confiança durante o desenvolvimento deste trabalho.

Ao meu orientador Professor Fábio Comes de Castro pela disponibilidade, paciência e atenção durante o desenvolvimento dessa dissertação e por todos ensinamentos transmitidos ao longo desses dois anos.

Aos amigos de sala Artur, Daniel, Natália, Maycol, Thiago, Vitória, Felipe e Sarah pelos momentos de descontração. Aos amigos Miguel, Gustavo e Remy, pelos ensinamentos na operação dos equipamentos do laboratório. Ao amigo Erick, pelas descontraídas conversas relacionadas tanto ao tema de fadiga por fretting quanto a outros temas diversos. Ao amigo Pedro, que inúmeras vezes me auxiliou durante as diversas etapas dessa pesquisa.

À Empresa Amazonense de Transmissão de Energia S.A. (EATE) e à CAPES pelo auxílio ao projeto.

# Abstract

In this work, fretting fatigue tests are conducted on two crossed wires made of aluminum alloy 6201-T81 taken from the All Aluminum Alloy Cable 900 MCM conductor. A nonlocal stress-based fatigue model, which was recently developed at the University of Brasilia, is evaluated in terms of its capability to predict the fatigue lives and the critical plane orientations of the wires. The elastic-plastic contact model used in the fatigue life prediction methodology is evaluated with respect to its capability to predict the sizes of the contact marks. The fatigue tests were performed on a four-actuator fretting apparatus in which the wires are pressed against each other by a constant normal force and one of the wires is subjected to a constant amplitude axial loading. The fatigue model uses an average stress over a damage zone to account for the high stress gradient beneath the contact surface. A stress-based version of the Smith, Watson, and Topper parameter with a critical plane interpretation is used to quantify the fatigue damage. The implication of adopting a linear elastic or an elastic-perfectly plastic material behavior in the contact model used for fatigue life prediction is investigated. It was observed that the lives of the wire specimens can be affected by the magnitudes of the normal force and mean axial force. A partial slip fretting regime was identified in all specimens and failures initiated at the extremity of the major axes of the contact marks. Fatigue lives estimated using the cyclic stresses outputted from the linear elastic contact model were overly conservative. On the other hand, the use of an elastic-perfectly plastic material behavior in the contact model significantly improved life estimation, with most of the estimated lives falling within factors of five of the observed lives. The fatigue model was capable of describing the early crack orientations observed in the wire specimens with reasonable accuracy. The sizes of the contact marks were also reasonably well predicted using the elastic-plastic contact model of the wires.

# Resumo

Neste trabalho, ensaios de fadiga por fretting são conduzidos em dois fios cruzados feitos da liga de alumínio 6201-T81 retirados de um Cabo de Alumínio Liga 900 MCM. Um modelo de fadiga não-local, que foi recentemente desenvolvido na Universidade de Brasília, é avaliado em termos de sua capacidade de prever vidas em fadiga e orientações de plano crítico dos fios. O modelo de contato elasto-plástico utilizado na metodologia de previsão de vida é avaliado em relação a sua capacidade de prever os tamanhos das marcas de contato. Os ensaios de fadiga foram realizados em um equipamento de fretting de quatro atuadores, onde os fios são comprimidos um contra o outro por uma força normal constante e um dos fios é submetido a um carregamento axial com amplitude constante. O modelo de fadiga usa uma tensão média sobre uma zona de dano para levar em conta o alto gradiente de tensão abaixo da superfície de contato. Uma versão baseada em tensão do parâmetro de Smith, Watson e Topper com uma interpretação de plano crítico é utilizada para quantificar o dano por fadiga. A implicação de se adotar um comportamento material linear elástico ou elástico-perfeitamente plástico no modelo de contato utilizado para previsão de vida em fadiga é investigada. Observou-se que as vidas dos corpos de prova de fios podem ser afetadas pelas magnitudes da força normal e da força média axial. Um regime de fretting de escorregamento parcial foi identificado em todos corpos de prova e as falhas iniciaram-se nas extremidades do maior eixo das marcas de contato. As vidas em fadiga estimadas utilizando as tensões cíclicas extraídas do modelo de contato linear elástico foram excessivamente conservativas. Por outro lado, o uso de um comportamento material elástico-perfeitamente plástico melhorou significativamente as estimativas de vida, estando a maior parte das vidas estimadas enquadradas em fatores de cinco das vidas observadas. O modelo de fadiga foi capaz de descrever as orientações iniciais das trincas observadas nos corpos de prova de fios com razoável acurácia. Os tamanhos das marcas de contato também foram previstos com razoável acurácia pelo modelo de contato elasto-plástico dos fios.

# CONTENTS

<b>1</b>	<b>INTRODUCTION</b> .....	<b>1</b>
1.1	MOTIVATION .....	1
1.2	OBJECTIVES .....	2
1.3	PUBLICATIONS .....	3
<b>2</b>	<b>FRETTING FATIGUE OF 6201 ALUMINUM ALLOY WIRES</b> .....	<b>4</b>
2.1	INTRODUCTION .....	4
2.2	EXPERIMENTAL PROGRAM .....	5
2.3	FATIGUE MODEL .....	11
2.4	FINITE ELEMENT-BASED STRESS ANALYSIS .....	16
2.5	RESULTS AND DISCUSSION .....	19
2.5.1	CHARACTERIZATION OF THE FRETTING REGIME .....	19
2.5.2	FRACTURE SURFACE EXAMINATION .....	21
2.5.3	COMPARISON OF OBSERVED AND ESTIMATED CRITICAL PLANE ORIEN- TATIONS .....	22
2.5.4	COMPARISON OF OBSERVED AND ESTIMATED LIVES .....	25
2.5.5	COMPARISON OF OBSERVED AND ESTIMATED CONTACT MARKS .....	27
<b>3</b>	<b>CONCLUSIONS</b> .....	<b>30</b>
	<b>REFERENCES</b> .....	<b>32</b>
	<b>APPENDICES</b> .....	<b>36</b>
<b>A</b>	<b>ENERGY-DISPERSIVE SPECTROSCOPY MAPPING OF THE CONTACT MARKS</b> .....	<b>37</b>
<b>B</b>	<b>OBSERVED CRITICAL PLANES</b> .....	<b>42</b>
<b>C</b>	<b>OBSERVED AND ESTIMATED CONTACT MARKS</b> .....	<b>47</b>

# List of Figures

1.1	(a) Transmission tower (Wikimedia, 2013), (b) suspension clamp and (c) contact marks found at inner layers of a conductor. ....	2
2.1	Tensile curve of the 6201-T81 aluminum alloy.....	6
2.2	Geometry and dimensions (in mm) of the plain and V-notched wire specimens....	6
2.3	$S-N$ curves of the plain and V-notched wire specimens. ....	7
2.4	Experimental apparatus used in the fretting fatigue tests on contacting wires: (a) overall view, (b) contact system and (c) detail of the contact region. ....	8
2.5	Schematic of the (a) applied loads and (b) loading history used in the wire-wire fatigue tests.....	9
2.6	Maximum stress versus fatigue life for the tests performed with normal loads of: (a) 500 N and (b) 750 N. ....	10
2.7	Maximum stress versus fatigue life for the tests performed with maximum stresses of 279 MPa, 266 MPa and 251 MPa ....	11
2.8	Schematic of the fatigue damage zone in the wire-wire fatigue tests. ....	13
2.9	Schematic of the procedure for obtaining the material constants of the $L-N_f$ relation. ....	15
2.10	Schematic of the procedure for estimating the fatigue life of the wire-wire fatigue tests. ....	16
2.11	FE model of wire with a circumferential sharp V-notch: (a) mesh with detail of the refined partition and (b) boundary conditions.....	17
2.12	FE model of the wire-wire experimental configuration: (a) mesh with detail of the refined partition and (b) boundary conditions.....	18
2.13	EDS of specimen no. 2 showing the presence of oxygen (blue) and aluminum (green) particles. ....	20
2.14	Fracture surface of the specimen no. 2. ....	21
2.15	Details of the striation marks and dimples found at the fracture surface of the specimen no. 2. ....	22
2.16	Schematic of the procedure to measure the critical plane orientation of the specimen no. 2.....	23
2.17	Final fracture surfaces observed on the wire specimens: (a) V-type of fracture in specimen no. 8 and (b) 45°-type of fracture in specimen no. 17 ....	25
2.18	Correlation between the characteristic length and the number of cycles to failure of the V-notched wires. ....	26

2.19	Observed lives of the wire-wire fatigue tests vs. estimates using the nonlocal SWT fatigue criterion.....	27
2.20	Comparison between the (a) observed and (b) estimated contact marks for the specimen no. 2. ....	28



# List of Tables

2.1	Summary of the wire-wire fatigue test data of AA6201-T81. ....	10
2.2	Comparison between observed and estimated critical plane orientations. ....	24
2.3	Observed and estimated dimensions of the contact marks.....	28

# Nomenclature

$A, b$	Material constants of the SWT- $N_f$ relation
$C, d$	Material constants of the $L$ - $N_f$ relation
$f$	Loading frequency
$F_m$	Mean force
$I_{2a}, I_{2b}$	Differences between observed and estimated major and minor axes of the contact marks
$L$	Critical distance
$N_f$	Number of cycles to failure
$N_L$	Fatigue life estimate associated with a critical distance $L$
$N_{\text{SWT}}$	Fatigue life estimated by using the SWT parameter
$P$	Normal force
$R$	Load ratio
$S_{\text{max}}$	Maximum nominal stress
SWT	Smith–Watson–Topper parameter
$V$	Volume of the fatigue damage zone
$\alpha$	Crossing angle between the wires
$\Delta F/2$	Force amplitude
$\Delta S/2$	Stress amplitude
$\sigma$	Average stress tensor
$\sigma_{\text{na}}$	Normal stress amplitude
$\sigma_{\text{nmax}}$	Maximum normal stress
$\hat{\sigma}$	Stress tensor
$\theta$	Orientation of the surface crack
$\phi$	Inclination of the crack

# 1 Introduction

## 1.1 Motivation

The present research work was carried out as part of a research project entitled “Fatigue of All Aluminum Alloy Cables 1120 AAAC and 6201 AAAC: Comparative study and effect of AGS clamps and conductive splicers”. This project is the result of a partnership between the University of Brasília and Transmissoras Brasileiras de Energia – TBE, and focuses on the development of experimental and numerical techniques to analyze the mechanical behavior and fatigue failure of overhead conductors and individual wires made of 1120 and 6201 aluminum alloys.

Over the last decade, one of the biggest challenges faced by the Brazilian energy industry was to interconnect the hydrographic basins located at the northern region of the country with the basins of the southeast and south regions with high voltage and ultra high voltage transmission lines (Guimarães and Miller, 2012). A crucial aspect considered in the construction of these lines is the load-to-weight ratio of the conductor. In this sense, the use of aluminum alloys 1120 and 6201 could be considered advantageous, because these alloys are used in All Aluminum Alloy Conductors, which are usually lighter than ACSR (Aluminum Conductor Steel Reinforced) conductors with similar dimensions (Barber and Callaghan, 1995; Hazan, 1970).

Another fundamental aspect in the transmission line design is to prevent wire ruptures, which are widely associated to the occurrence of fretting (Ouaki et al., 2003; Zhou et al., 1994; Fricke and Rawlins, 1968), a surface damage induced by minute relative displacement between contacting surfaces (Hills and Nowell, 1994). As a matter of fact, this phenomenon was observed to be the main cause of failure in a 460 kV transmission line crossing the Paraná River (Azevedo and Cescon, 2002), as well as of a 230 kV transmission line located at the Center-West region of Brazil (Kalombo et al., 2015).

To understand how fretting can cause the failure of a transmission line, consider a typical transmission tower, such as the one shown in Fig. 1.1a. Components like the suspension clamp shown in Fig. 1.1b are placed on the cross arms of the tower and are used to support the conductors. Near the regions where the components clamp the conductor, a combination of static and time-varying stresses is developed due to the weight of the conductor, the clamping force, and the vibration induced by the wind, among other factors. These load conditions favor the occurrence of fretting between contacting surfaces. This effect can be verified at the elliptical contact marks produced in the contact between wires of adjacent layers, as presented in Fig. 1.1c. Some of these marks (A) may present a dark layer, formed by particles that are detached from the contacting surfaces and oxidized during the fretting process. These particles

favor crack initiation at the contact zones and can eventually lead to wire ruptures (B). Therefore, the study of failures in transmission lines involves understanding the local fretting process that takes place in the contact between wires.

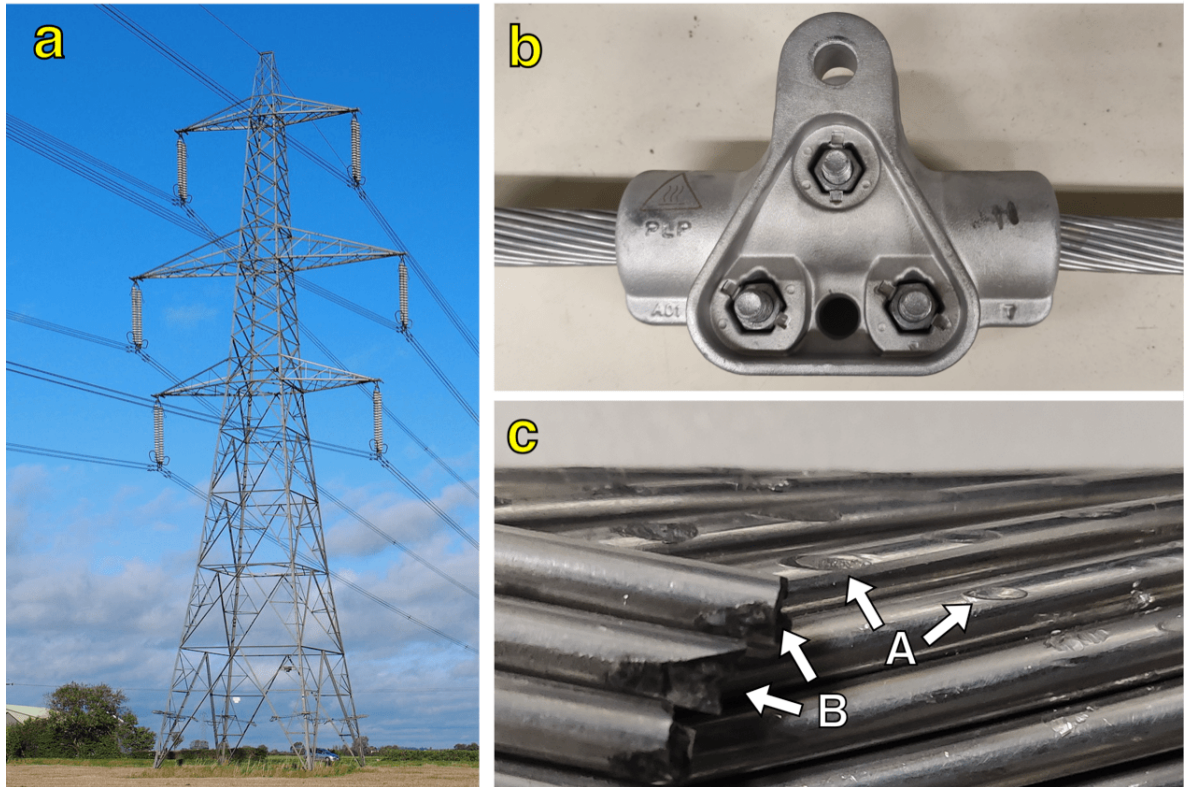


Figure 1.1: (a) Transmission tower (Wikimedia, 2013), (b) suspension clamp and (c) contact marks found at inner layers of a conductor.

## 1.2 Objectives

Recent studies have tried to understand fatigue failures of overhead conductors from a local point of view, either by performing fatigue tests or by modeling the fatigue damage on two contacting wires (Said et al., 2020; Rocha et al., 2019; Díaz, 2018; Ma et al., 2017; Zhao et al., 2011). In particular, Rocha et al. (2019) proposed a critical plane fatigue model to predict the fatigue life of contacting wires, which provided life predictions within factor-of-three boundaries for 1350-H19 aluminum alloy wires. The promising results obtained with this fatigue model have motivated the research group of the University of Brasilia to further evaluate it. Within this context, the specific objectives of this work are:

- (1) To produce new test data by conducting fretting fatigue tests on wires made of 6201-T81 aluminum alloy.
- (2) To further develop the life prediction methodology of Rocha et al. (2019) by incorporating an elastic-plastic constitutive behavior into the wire-wire contact model.

- (3) To evaluate the critical plane fatigue model in terms of its capability to predict the lives and critical planes observed in the wire-wire fatigue tests.
- (4) To evaluate the capability of the elastic-plastic contact model to estimate the size of the contact marks.

## **1.3 Publications**

The following papers have been based on work contained in this Master Dissertation:

In International Journal:

Araújo J. A., Castro F. C., Matos I. M., Cardoso R. A., 2020. Life prediction in multiaxial high cycle fretting fatigue. *International Journal of Fatigue*, Vol. 134, pp. 105504.

In International Conference:

Matos I. M., Rocha P. H. C., Araújo J. A., Castro F. C., 2019. Fatigue life prediction of AA1350-H19 wire under high stress gradient. *Proceedings of the 7th International Symposium on Solid Mechanics - MECSOL 2019*.

# 2 Fretting fatigue of 6201 aluminum alloy wires

## 2.1 Introduction

Overhead conductors are frequently subjected to aeolian vibration, which may lead to the fatigue failure of the conductor (IEEE, 2015). The failure usually takes place near components where the movement of the conductor is restrained, such as suspension clamps, spacer dampers, vibration dampers and strain clamps (Chen et al., 2012; Fadel et al., 2012; Azevedo and Cescon, 2002; Cardou et al., 1990; McGill and Ramey, 1986). In these regions, individual wires may be subjected to a complex combination of time-varying stresses due to aeolian vibration, and static stresses caused by the clamping pressure, stretching load and weight of spans. Such conditions favor the occurrence of fretting fatigue, which may lead to the rupture of the wires (Azevedo et al., 2009).

Traditional studies on the fatigue behavior of overhead conductors are performed using test benches. These studies are particularly useful to understand the fretting problem in transmission lines on a global scale, especially concerning the conductor-clamp assembly. For example, such type of studies has indicated that wire ruptures usually occur due to fretting, that the fretting regime can change depending on the longitudinal position of the fretting mark, and that there is a critical region in the conductor-clamp assembly where wire breaks are most frequent (Ouaki et al. 2003; Zhou et al., 1994). This type of test is also useful to better understand the factors that can affect the fatigue performance of the conductor, such as clamp geometry (McGill and Ramey, 1986) mean load (Fadel et al., 2012; Cardou et al., 1990) and vibration amplitude (Ouaki et al. 2003; Zhou et al., 1994).

More recent studies have analyzed the fretting behavior of overhead conductors on a local scale, in an attempt to reproduce the fretting condition that occurs at the contact between two wires of adjacent layers of the conductor. To accomplish this, fretting tests are performed with two crossed wires compressed into each other. One of the wires is fixed, while the other is subjected to a fatigue load or cyclic displacement that causes the fretting condition (Said et al., 2020; Rocha et al., 2019; Díaz, 2018; Ma et al., 2017; Zhao et al., 2011). This approach can complement the usual tests with conductors and provide a better understanding of the fretting phenomenon in individual contacts. These studies have shown that the fatigue life of contacting wires can be affected by compressive force, fatigue loading and crossing angle between the wires (Díaz, 2018; Zhao et al., 2011), and that a corrosive atmosphere can affect wear damage and fretting regime (Ma et al., 2017). Some efforts have also been directed to the development

of numerical models for contacting wires, allowing the prediction of contact pressure, area of contact and region of crack initiation (Said et al., 2020; Lévesque et al., 2011).

In a recent work conducted at the University of Brasilia (Rocha et al., 2019), a nonlocal fatigue model capable of predicting the fatigue life of fretting wires was proposed. This model used an average stress to account for the high stress gradient beneath the contact surface, and the Smith, Watson, and Topper parameter to quantify the fatigue damage. The model was capable of making fatigue life predictions of 1350-H19 aluminum alloy contacting wires within factor-of-three boundaries. In what follows, this model is further evaluated by means of new wire-wire fatigue tests performed on 6201-T81 aluminum alloy wires. In addition to the linear elastic constitutive behavior adopted by (Rocha et al., 2019), an elastic-plastic behavior is also incorporated into the wire-wire contact analysis. Fatigue lives and crack initiation planes are estimated and compared with results from the wire-wire tests. The size of the contact marks is also estimated by the elastic-plastic contact model and compared to experimental observations.

## **2.2 Experimental program**

The material used in this study is the aluminum alloy (AA) 6201-T81. This alloy was originally designed to be used in overhead conductors at marine environments, replacing the 6/1 Aluminum Conductor Steel Reinforced (ACSR) which suffered from bimetallic corrosion. An All Aluminum Alloy Cable (AAAC) was then developed using the AA6201, providing a conductor with electrical conductivity and mechanical resistance comparable to a same-sized 6/1 ACSR, but lighter and with higher corrosion resistance (Hazan, 1970; Greenfield, 1959). Nowadays, this material is still widely used in overhead conductors (Kalombo et al., 2015; Rhaïem et al., 2010) as it is lighter, more resistant and more conductive than ACSR conductors of equal diameter (Karabay, 2006).

The chemical composition of the AA6201-T81 in weight percentage is 98.54 Al, 0.65 Mg, 0.58 Si, 0.21 Fe and 0.0032 B (Adriano et al., 2018). Fig. 2.1 shows the monotonic tension curve of the material from which the following properties were obtained: Young's modulus of 69 GPa, yield stress of 306 MPa, and ultimate tensile strength of 311 MPa. Note that the tensile behavior of the material is approximately elastic-perfectly plastic.

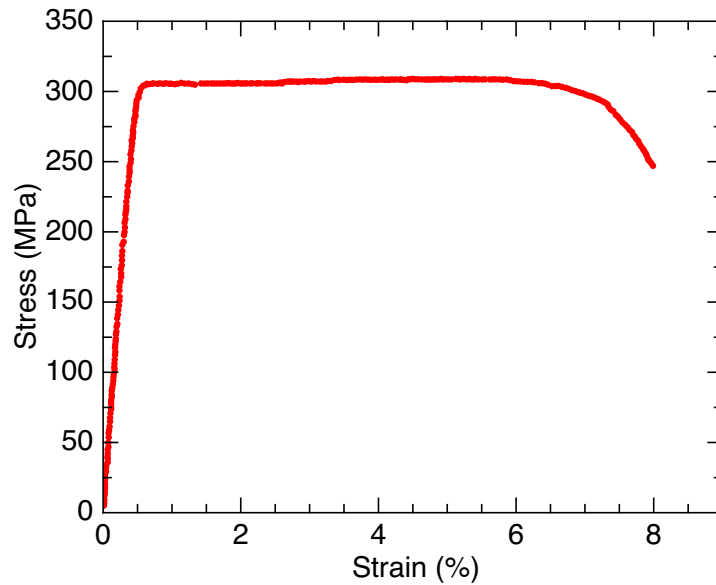


Figure 2.1: Tensile curve of the 6201-T81 aluminum alloy.

Previously obtained data from uniaxial fatigue tests on AA6201-T81 wire specimens (Adriano et al., 2018) will be used later to calibrate the fatigue model. Such tests were conducted using 3.96 mm diameter wires taken from an All Aluminum Alloy Cable (AAAC) 900 MCM conductor. The plain and V-notched wires were subjected to fully reversed axial loading, with loading frequencies ranging from 10 to 40 Hz. Failure was defined as the complete rupture of the specimens and run out as  $5 \times 10^6$  cycles. Geometry and dimensions of the specimens are presented in Fig. 2.2, and the stress-life curves are expressed in Fig. 2.3 in terms of the stress amplitude  $\Delta S/2$  in the net cross-sectional area.

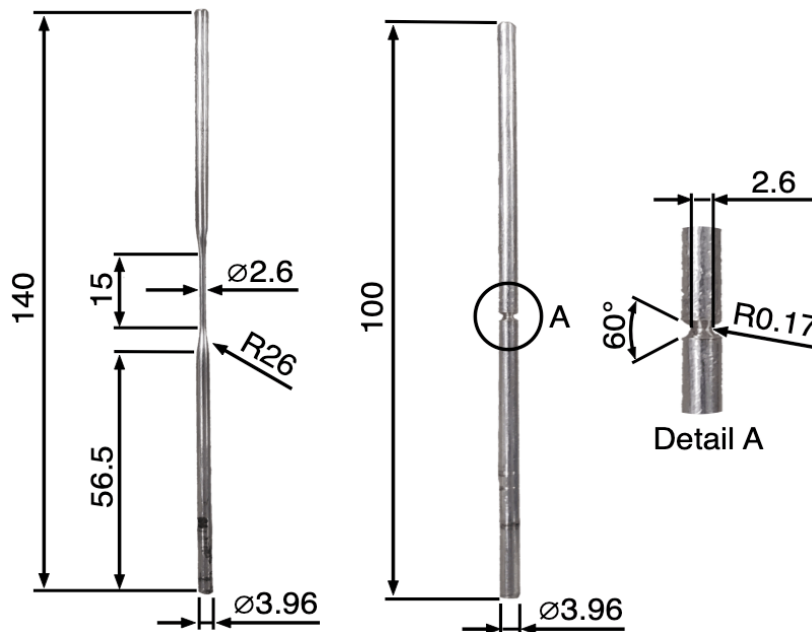


Figure 2.2: Geometry and dimensions (in mm) of the plain and V-notched wire specimens



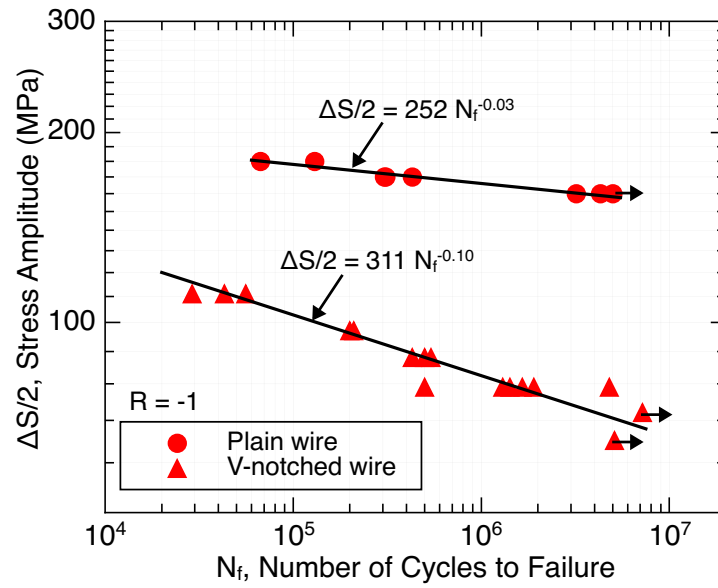


Figure 2.3:  $S$ - $N$  curves of the plain and V-notched wire specimens.

New fretting fatigue tests on AA6201-T81 wires were conducted on the experimental apparatus shown in Fig. 2.4. This device is composed of two hydraulic and two pneumatic actuators. The upper hydraulic actuator (1) controls the vertical displacement of the contact system shown in Fig. 2.4b, and may be used to impose a tangential force to the system. In the interior of the carcass (2) is the lower hydraulic actuator, used to apply the fatigue loading to one of the wires (6). The contact system contains opposing pneumatic actuators (3), which push movable blocks (4) over tracks. One of the blocks contains a support with the other wire (5), while the other block contains a support with a bearing (7). With this contact system, it is possible to push one of the wires into the other and use the bearing to resist the compressive load. Further details on the experimental apparatus can be found in (Garcia, 2019)

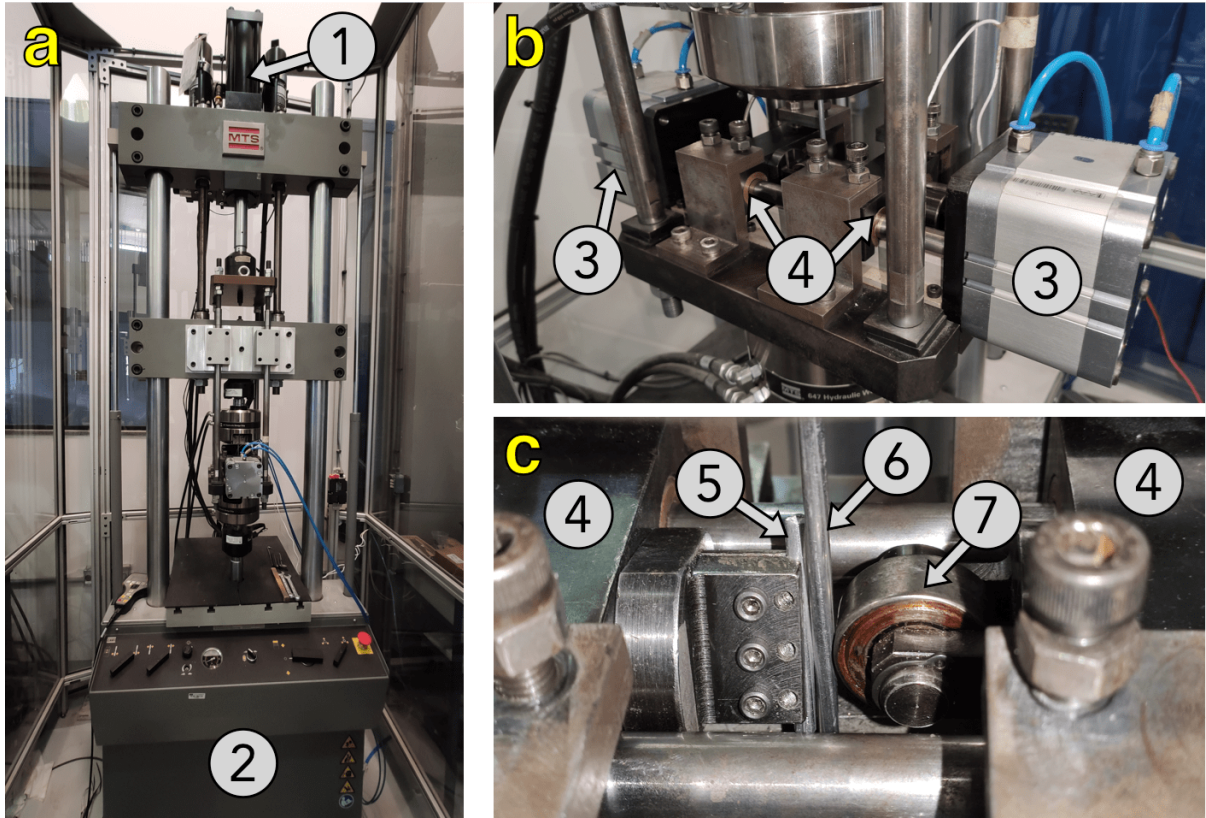


Figure 2.4: Experimental apparatus used in the fretting fatigue tests on contacting wires: (a) overall view, (b) contact system and (c) detail of the contact region.

All wire-wire fatigue tests were conducted following the loading condition illustrated in Fig. 2.5. First, one of the wires (specimen) is fixed by the hydraulic grips and the lower hydraulic actuator imposes a mean force  $F_m$  to one end of the specimen. Then, the other wire (pad) is positioned at the pad support with a certain crossing angle to the specimen. Both wires and the bearing are clamped into each other by a constant compressive force  $P$  applied by the pneumatic actuators. Finally, the specimen is subjected to a fatigue loading of constant amplitude  $\Delta F/2$ , applied by the lower hydraulic actuator.

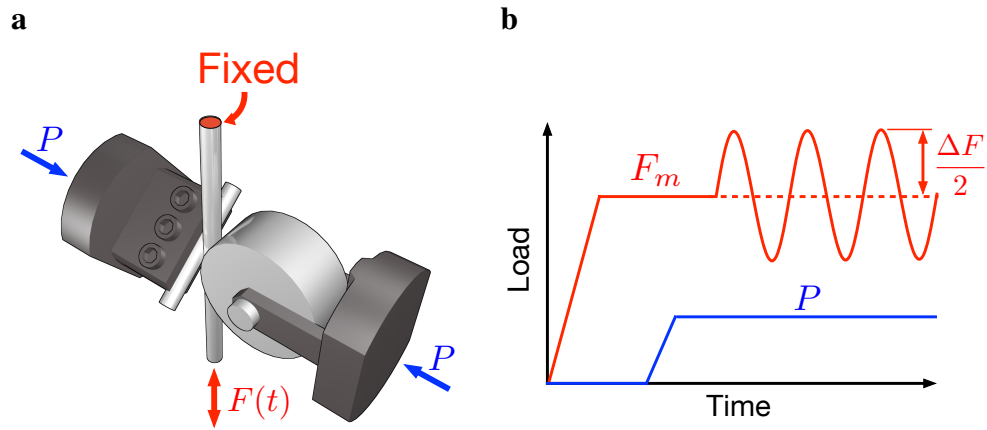


Figure 2.5: Schematic of the (a) applied loads and (b) loading history used in the wire-wire fatigue tests.

To define the magnitude of the loads applied to the wires in the fretting fatigue tests, the experimental-numerical methodology performed by Rocha (2019) was used. The researcher conducted fatigue tests on an AAAC 900 MCM conductor in a 47 m test bench. The critical region for fatigue failure (between the keeper edge and last point of contact between conductor and clamp) was instrumented with strain gages and the measured strains were used to estimate the stresses. To determine the compressive forces between the wires, the dimensions of the contact marks in the critical region were measured and finite element simulations were performed to replicate such dimensions. From this methodology, it was estimated that at the critical region of the conductor, the crossing angle between the wires was approximately  $20^\circ$ , the mean force ranged from 950 N to 2990 N, the force amplitude ranged from 268 N to 292 N and the compressive force ranged from 100 N to 1280 N.

Based on the loading magnitudes estimated by Rocha's methodology, the fretting tests were performed using a crossing angle of  $20^\circ$ , a force amplitude of 292 N and a compressive force of either 500 N or 750 N. The mean force ranged from 2490 N to 3150 N, resulting in load ratios of approximately 0.8. Table 2.1 shows a summary of the experimental parameters and observed fatigue life of each test, where the following nomenclature is adopted:  $P$  is the normal force,  $\Delta F/2$  and  $F_m$  are, respectively, the force amplitude and mean force of the fatigue loading,  $S_{max}$  is the maximum nominal stress,  $R$  is the load ratio,  $f$  is the loading frequency and  $N_f$  the number of cycles to failure. The maximum stress versus fatigue life data were also plotted in Fig. 2.6.

Table 2.1: Summary of the wire-wire fatigue test data of AA6201-T81.

Specimen ID	$P$ [N]	$\Delta F/2$ [N]	$F_m$ [N]	$S_{max}$ [MPa]	$R$	$f$ [Hz]	$N_f$ [cycles]
01	500	292	3150	279	0.83	15	985,499
08	500	292	2990	266	0.82	27	1,350,201
24	500	292	2990	266	0.82	27	1,572,473
23	500	292	2800	251	0.81	27	730,520
02	500	292	2800	251	0.81	20	2,844,101
11	500	292	2600	235	0.80	27	853,072
25	500	292	2600	235	0.80	27	>5,000,000
04	500	292	2490	226	0.79	20	>5,000,000
17	750	292	3150	279	0.83	27	4,610,117
06	750	292	3150	279	0.83	27	4,773,894
18	750	292	2990	266	0.82	27	>11,513,988
10	750	292	2800	251	0.81	27	4,640,891

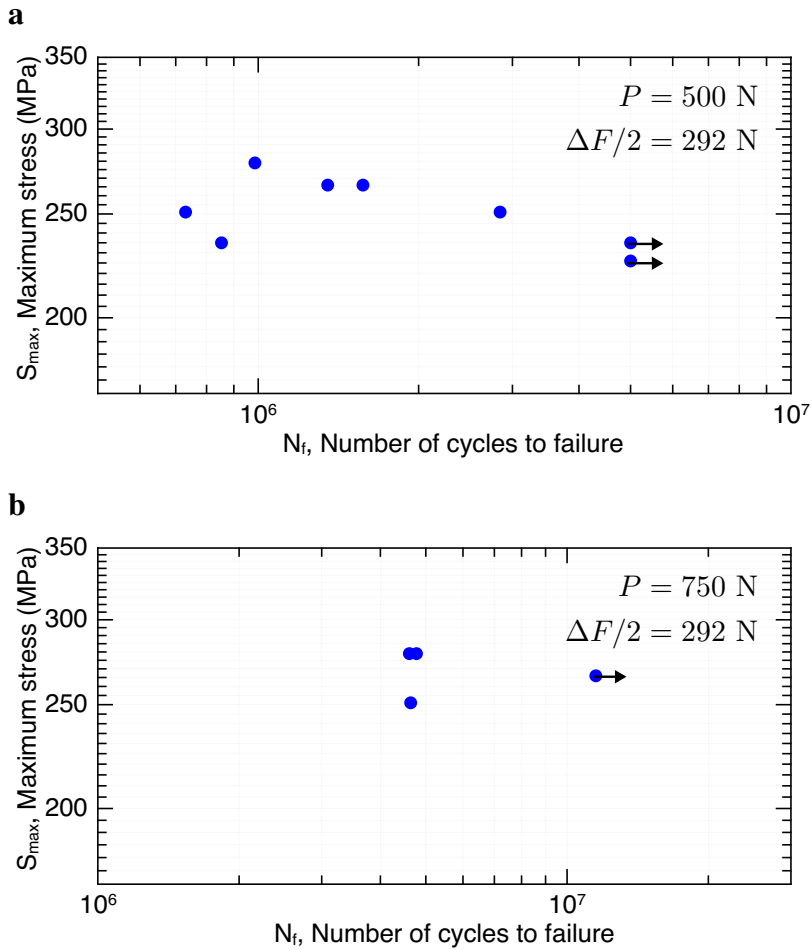


Figure 2.6: Maximum stress versus fatigue life for the tests performed with normal loads of: (a) 500 N and (b) 750 N.

For the tests performed with a compressive force of 500 N, it can be seen in Fig. 2.6a that the maximum stress can affect the fatigue life of the wires. For example, the fatigue life observed on the test with a maximum stress of 226 MPa is more than five times higher than the one verified in the test with a maximum stress of 279 MPa. Considering that the force amplitude is the same for all tests, lower mean forces generally provided longer fatigue lives. However, for the tests shown in Fig. 2.6b with a compressive force of 750 N, no clear correlation can be observed between the mean force and the fatigue life. Further tests are required to better evaluate this effect.

The effect of the normal load on the fatigue life of the wires can be observed graphically in Fig. 2.7, which shows the  $S$ - $N$  data points for tests performed with maximum stresses of 279 MPa, 266 MPa and 251 MPa. Open and solid symbols represent tests performed with a normal loads of 500 N and 750 N, respectively. A vertical dashed line was drawn at  $N_f = 4 \times 10^6$  cycles to better visualize the data. It is clear that tests with a normal load of 750 N presented higher fatigue lives than the ones with 500 N for all of the mean loads analyzed.

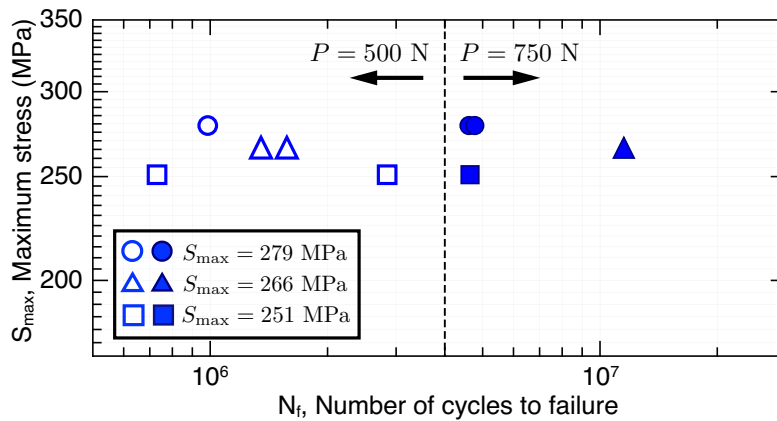


Figure 2.7: Maximum stress versus fatigue life for the tests performed with maximum stresses of 279 MPa, 266 MPa and 251 MPa

## 2.3 Fatigue model

The problem of fretting fatigue of wires may present high stress gradients due to the localized stress concentration at the contact. As high stress gradients also occur in sharp notches, it seems reasonable to try to apply life prediction methodologies traditionally used in notched members to wires. A widely used method for life prediction of notched members is the Theory of Critical Distances (TCD), which was originally developed by Neuber (1958) and Peterson (1959) and later improved by Taylor (1999). The underlying assumption in their works is that the fatigue strength of notches is determined by the average stress over a damage zone surrounding the hot-spot, whose size is defined by a critical distance  $L$ .

The determination of the critical distance from fatigue test data is an important aspect for the successful use of life prediction methodologies based on the TCD. In the Neuber and

Peterson's formulations, the critical distance is determined by means of empirical relations. To improve the original TCD, Taylor (1999) proposed to identify the critical distance by fitting fatigue limit data of a specimen containing a sharp notch or a crack. An extension of the original work of Taylor (1999) to the prediction of fatigue life was proposed by Susmel and Taylor (2007). In this approach, the critical distance is not regarded as a constant, but as a variable related to the number of cycles to failure by a power-law relation given by

$$L = CN_f^d \quad (2.1)$$

where  $C$  and  $d$  are material parameters that can be obtained by fitting  $S$ - $N$  curves of specimens containing a sharp notch.

In the present work, the TCD is used in its volumetric form in which the average stress tensor  $\sigma$  over a fatigue damage zone is defined by

$$\sigma = \frac{1}{V} \int_V \hat{\sigma} dV \quad (2.2)$$

where  $\hat{\sigma}$  is the stress tensor at a point within the volume  $V$  of the fatigue process zone. The damage zone was chosen as a hemisphere of radius  $L$  whose center of the flat side is located at the hot-spot. For the wire-wire fatigue analysis, the hot-spot is located at the lower extremity of the major axis of the contact zone (point A in Fig. 2.8). This point was chosen as the hot-spot based on previous studies (Garcia, 2019; Díaz, 2018) that have identified it as the crack initiation site. Furthermore, Rocha (2019) performed fatigue analyses in which the center of the flat side of the hemispherical damage zone was positioned at the upper and lower extremities of the major axis, and at the center of the contact zone, and concluded that fatigue damage was critical at the lower extremity.

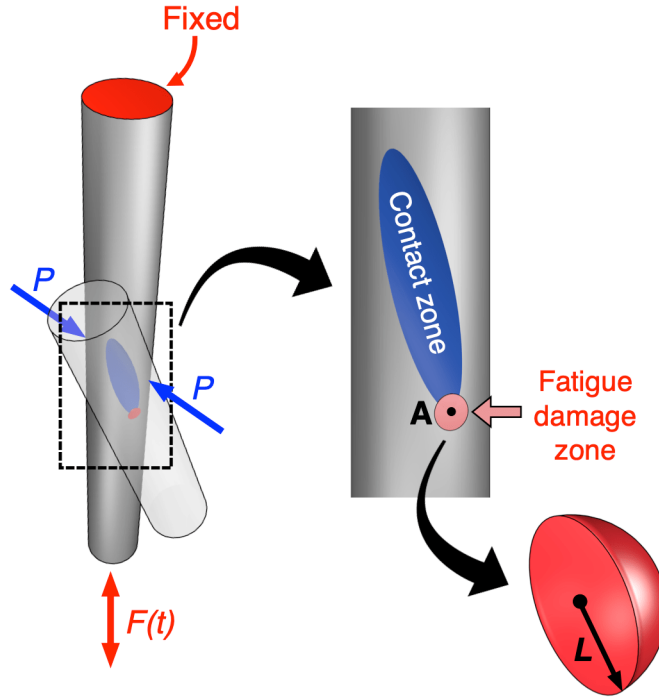


Figure 2.8: Schematic of the fatigue damage zone in the wire-wire fatigue tests.

The stress field generated by the contact of wires has a multi-axial nature. Among the different approaches for fatigue life prediction under multi-axial loading conditions, critical plane fatigue criteria are widely accepted for fatigue damage evaluation. These criteria are based on physical observations that indicate that cracks are formed and grow on preferred planes, whose orientation depends on the material and loading conditions (Fatemi and Shamsaei, 2011).

In this work, fatigue damage is quantified using a stress-based version of the Smith, Watson and Topper (SWT) parameter with a critical plane interpretation (Smith et al., 1970; Socie, 1987). The SWT parameter can be written as

$$\text{SWT} = \sqrt{\sigma_{\text{na}} \langle \sigma_{\text{nmax}} \rangle} \quad (2.3)$$

where  $\sigma_{\text{na}}$  is the normal stress amplitude and  $\sigma_{\text{nmax}}$  is the maximum normal stress in a loading cycle. The critical plane is defined as the material plane where the fatigue parameter is maximum. Note that Eq. (2.3) is the stress-based version of the original stress-strain-based SWT parameter. It is applicable in the high cycle fatigue regime, when plastic strain is small or negligible or after an elastic shakedown state has been achieved. The symbol  $\langle \rangle$  represents the Macaulay brackets defined as  $\langle x \rangle = 0.5(x + |x|)$ . To calculate the fatigue parameter, the history of the average stress tensor defined in Eq. (2.2) is used as input data. The use of the Macaulay brackets ensures that no negative damage can be produced.

To relate the SWT parameter with the fatigue life, the following power-law function is

used:

$$\text{SWT} = AN_f^b \quad (2.4)$$

where  $A$  and  $b$  are material constants obtained by best fitting the  $S$ - $N$  test data from plain specimens.

The procedure used to obtain the constants  $C$  and  $d$  of Eq. (2.1) can be summarized in the following steps. Initially, one point is chosen from the fatigue test data of the notched specimen, providing a pair of stress amplitude,  $\Delta S/2$ , and observed fatigue life,  $N_{\text{obs}}$ . Then, a trial value for the radius  $L_{\text{trial}}$  of the semi spherical fatigue damage zone is estimated, and a finite element simulation of the fatigue test is performed. The stress history can be extracted from this simulation and used to calculate the average stress with Eq. (2.2). This average stress can then be used to identify the material plane that maximizes the SWT fatigue parameter given in Eq. (2.3) and this parameter can be applied in Eq. (2.4) to obtain a fatigue life estimate,  $N_{\text{SWT}}$ . If the life estimate is equal to the observed fatigue life ( $N_{\text{SWT}} = N_{\text{obs}}$ ), then the estimated radius of the semi spherical damage zone is the critical distance,  $L$ , for the observed fatigue life,  $N_{\text{obs}}$ . Otherwise, the procedure is repeated using a different radius for the damage zone until the estimated and observed lives are the same. After repeating this procedure for all of the test data of the notched specimen, the results can be expressed in a  $L$ - $N_f$  curve and parameters  $C$  and  $d$  of Eq. (2.1) can be obtained.

A similar procedure can be used to obtain life predictions of the wire specimens used in the wire-wire fatigue tests. The loading conditions from one of the wire-wire fatigue tests are chosen, and a finite element simulation is performed using a semi-spherical damage zone with an trial radius  $L_{\text{trial}}$ . The stress history extracted from this damage zone is used to determine an average stress, which is applied in Eq. (2.4) to obtain a fatigue life estimate  $N_{\text{SWT}}$ . Here, a second life estimate,  $N_L$ , is obtained using the  $L$ - $N_f$  relationship, given in Eq. (2.1). If both fatigue life estimates are equal ( $N_{\text{SWT}} = N_L$ ), then the estimated value is the fatigue life estimate for the chosen loading conditions. Otherwise, the procedure is repeated using a different radius for the damage zone.

Schematics of the procedures used for obtaining the material parameters of the  $L$ - $N_f$  relationship and for estimating the fatigue lives of the wire specimens used in the wire-wire fatigue tests are presented in Figs. 2.9 and 2.10, respectively.



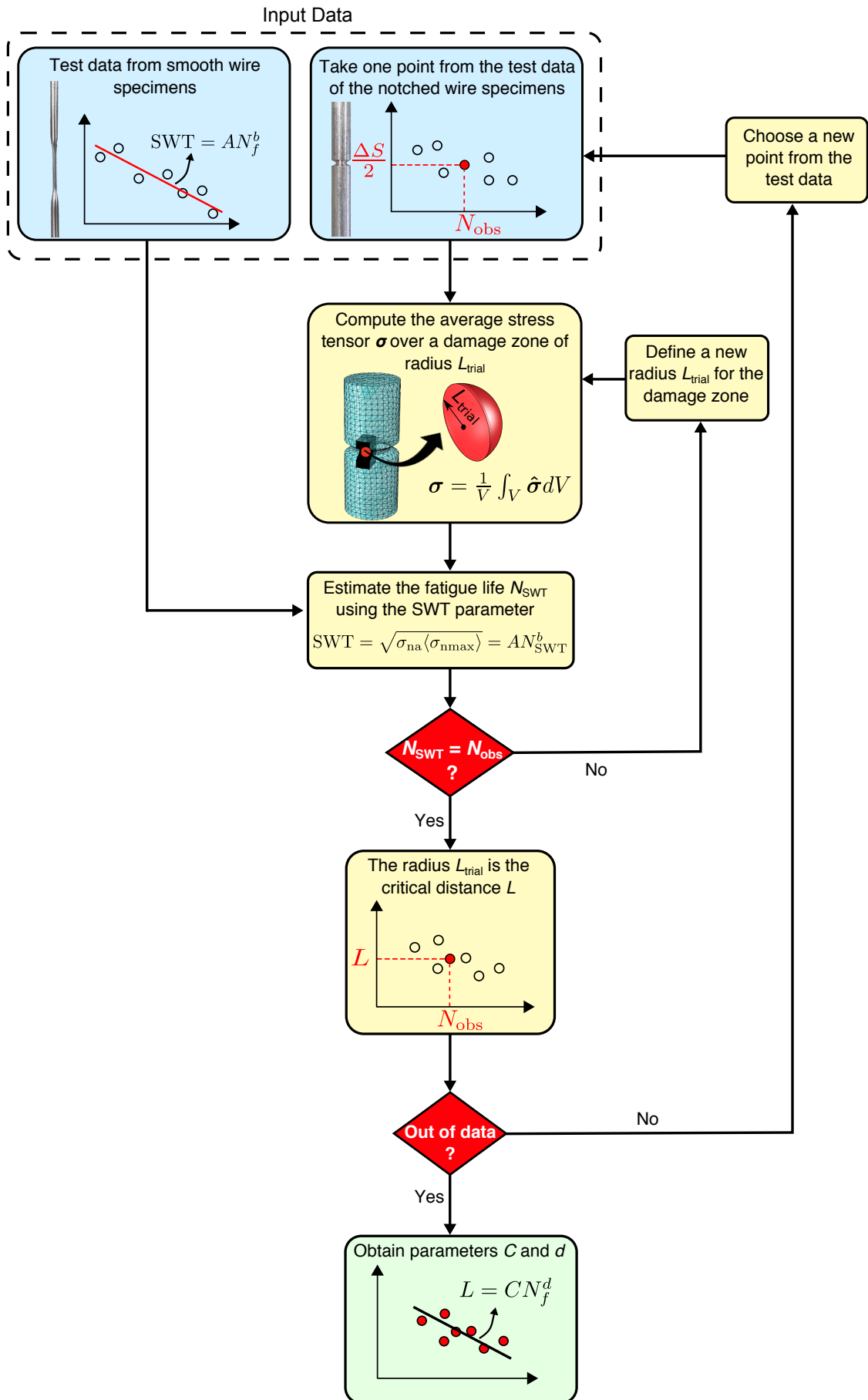


Figure 2.9: Schematic of the procedure for obtaining the material constants of the  $L-N_f$  relation.

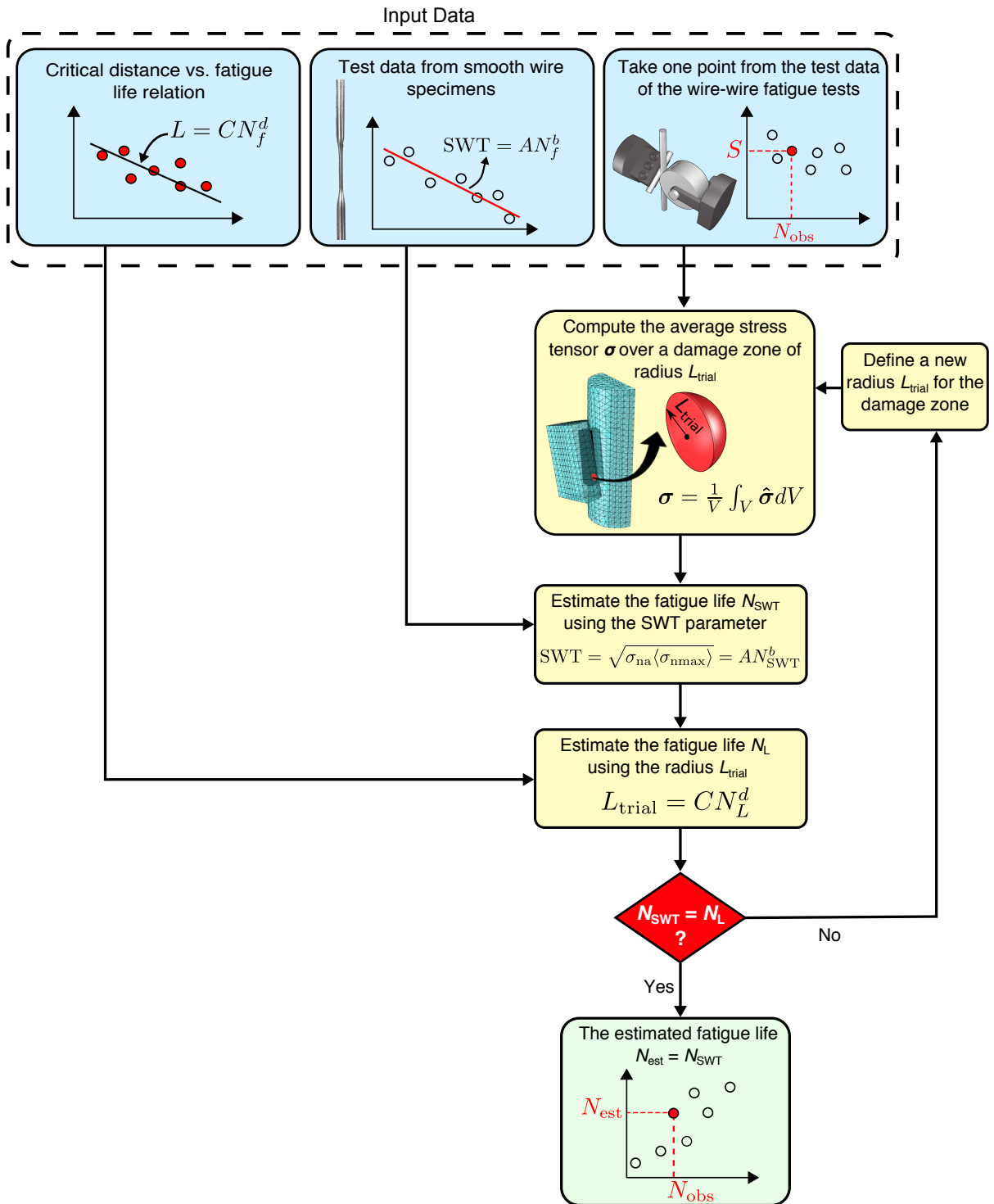


Figure 2.10: Schematic of the procedure for estimating the fatigue life of the wire-wire fatigue tests.

## 2.4 Finite element-based stress analysis

A fatigue model, which can be used to predict the fatigue life of contacting wires was presented in Section 2.3. The model needs to be calibrated using fatigue test data from not-

ched specimens. In both procedures of model calibration and life prediction, it is necessary to describe the stress distribution in the fatigue damage zone and, to do so, finite element (FE) simulations were performed using the FE software Abaqus. Two different FE models were employed in these simulations. The first one is a model of the V-notched wires, used in the calibration procedure, while the second one is a model of the wire-wire tests, used in the life prediction procedure.

The FE model of the V-notched wire consisted of a cylinder with a diameter of 3.96 mm and a length of 10 mm. The cylinder has a circumferential V-notch, with dimensions according to the specifications of Fig. 2.2. A linear elastic material behavior was used in all simulations, defined by a Young's modulus of 69 GPa and a Poisson's ratio of 0.33. The mesh of the model is presented in Fig. 2.11a. A refined partition with approximate dimensions of 1x2x1.5 mm was used to better describe the stress field in the vicinity of the notch root. This partition contains a structured mesh, composed of eight-node linear brick elements with reduced integration (C3D8R) and approximate global size of 20  $\mu\text{m}$ . For the bulk of the wire, a more coarse, non-structured mesh was used, consisting of ten node quadratic tetrahedral elements (C3D10) with an approximate global size of 1 mm. To associate the bulk of the wire with the partition, a tie constraint option was used to tie the surfaces of the partition in contact with the bulk. This option ties two surfaces together, ensuring there is no relative displacement between them, and can be used even when the surfaces contain distinct meshes.

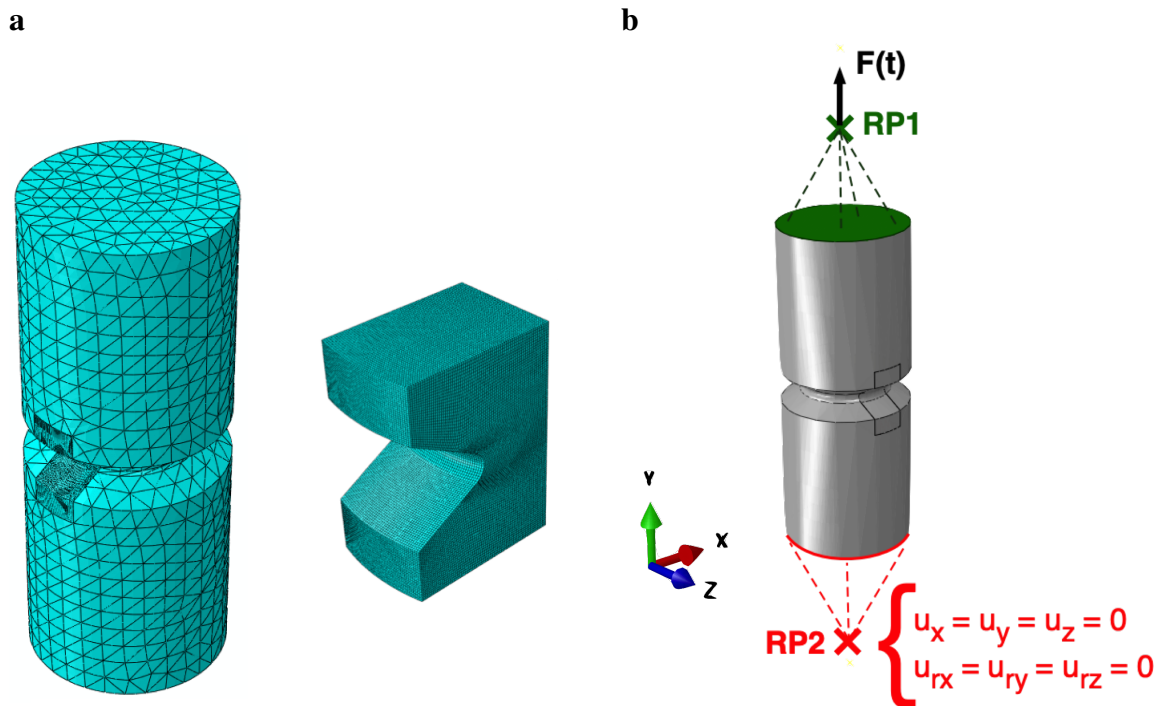


Figure 2.11: FE model of wire with a circumferential sharp V-notch: (a) mesh with detail of the refined partition and (b) boundary conditions.

Loading and boundary conditions were applied as represented in Fig. 2.11b. The upper and lower surfaces of the model were each associated with a different reference point. This association was achieved by using the coupling constraint, which prescribes individual weight factors to associate the loads applied to a reference point with the nodes of the surface. The fatigue loading is applied to reference point “RP1”, using the loading conditions of one point in the  $S-N$  curve. In reference point “RP2”, an encastre condition was imposed.

The finite element model of the contacting wires is composed of two half-cylinders with a diameter of 3.96 mm. One of the half-cylinders has a length of 10 mm and represents the specimen, while the other has a length of 5 mm and represents the pad. Both are placed in contact with each other at a crossing angle of  $20^\circ$ . The coordinate system is positioned at the surface of the specimen in contact with the pad, with the Y axis parallel to the axis of the specimen. Simulations were performed considering the load conditions presented in Table 2.1 and both a linear elastic and an elastic-perfectly plastic models. The linear elastic behavior was defined using the same parameters presented for the FE model of the V-notched wire, while the elastic-perfectly plastic behavior was defined using a yield stress of 306 MPa. The mesh used in the model is shown in Fig. 2.12a. In both specimen and pad, a partition is defined at the contact region, to better describe the stresses beneath the contact zone. The partitions for both models have the same dimensions, with an approximate size of  $0.8 \times 3.5 \times 0.6$  mm. The mesh in these regions is composed of eight-node linear brick elements with reduced integration (C3D8R) and approximate global size of  $16 \mu\text{m}$ . For the bulk of the specimen and pad, ten node quadratic tetrahedral elements (C3D10) with approximate global size of 0.4 mm are used.

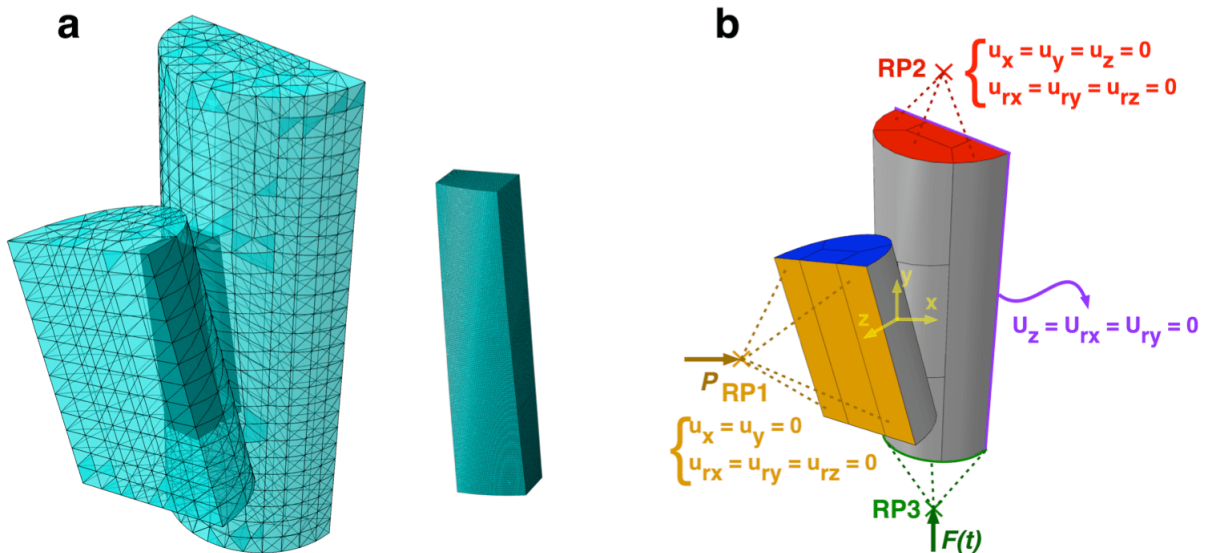


Figure 2.12: FE model of the wire-wire experimental configuration: (a) mesh with detail of the refined partition and (b) boundary conditions.

Loading and boundary conditions were defined as represented in Fig. 2.12b. The compressive force  $P$  is applied to the back surface of the pad using reference point “RP1”. At this point, a restraining condition is imposed to guarantee that the pad can only move along

the Z axis. To resist the compressive force, a condition of no displacement in the Z axis and no rotations about the X and Y axes is imposed on the back surface of the specimen. An encastre condition is imposed on reference point “RP2”, associated with the upper surface of the specimen and the fatigue loading,  $F(t)$ , is applied to the lower surface of the specimen.

The contact between the wires was described using finite sliding and a surface-to-surface contact discretization, which designates the contact between the specimen (master) and the pad (slave) partitions. The normal behavior of the contact was determined using a “hard” contact relationship to define the pressure-overclosure field. This relationship minimizes the penetration of slave nodes into the master surface. For the tangential behavior, friction was defined using the penalty formulation with a constant friction coefficient of 0.6.

## 2.5 Results and discussion

### 2.5.1 Characterization of the fretting regime

To implement the fatigue model presented in Section 2.3 and obtain fatigue life estimates for the wire-wire tests, the center of the flat side of the hemispherical damage zone was positioned at the extremity of the major axis of the contact zone. The position of this damage zone is based on the assumption that cracks initiate at this point and propagate due to the fatigue loading. This usually occurs when a partial slip regime is developed on the contact zone, since a micro slip zone is formed at the edge of the contact mark and cracks tend to initiate at this slip zone. To ensure that a partial slip fretting regime occurred in the wire-wire fatigue tests, Energy Dispersive Spectroscopy (EDS) was performed on the wire specimens.

In a typical conductor-clamp assembly, marks observed in the contact between wires can present three distinct contact behaviors. Beneath the keeper, marks are usually adhered because of the high pressure produced by the clamp. Further from the keeper, some marks present stick and micro slip zones. In the stick zone, there is no relative displacement between the surfaces. However, at the edges of the contact mark, a micro slip zone is formed and, because of the friction, aluminum particles are detached from the contacting surfaces. These particles react with the air of the environment, forming aluminum oxide ( $Al_2O_3$ ) debris. These dark particles have a hardness of approximately 2000 HV, significantly higher than that of the wires (for example, tests performed in our research lab provided a hardness of 87 HV for the AA6201-T81 wires). Therefore, the  $Al_2O_3$  particles act as abrasive materials, favoring crack initiation in the micro slip zones and propagation due to the cyclic loading. Even further from the keeper, the contact marks are completely worn-out and  $Al_2O_3$  particles are found at the whole contact zone. In such cases, cracks may initiate but vanish due to wear before they propagate (Azevedo et al., 2009; Ouaki et al., 2003; Aggarwal et al., 2000).

The results observed in the conductor-clamp assembly indicate that three different contact conditions could be observed in the contact marks: Adhesion, partial slip, and gross sliding.

To verify which condition happened in the wire-wire fatigue tests, an Energy-dispersive Spectroscopy (EDS) was performed. In this procedure, the microscope projects an X-ray into the specimen, causing the electrons in the atoms of the surface to transition from higher to lower energy levels, emitting electromagnetic radiation. The microscope measures the energy and quantity of the radiation emitted by the specimen during this transition and, because each chemical component has a unique atomic structure, it can differentiate the components by their emission spectrum. The way EDS can identify the contact condition is by assessing the number of oxygen particles present in the contact marks and their distribution. In the case of adhesion,  $Al_2O_3$  particles aren't formed and, therefore, a small number of oxygen atoms should be observed. For the partial slip, it is expected that oxygen atoms be concentrated at the edges of the contact mark, in the regions of micro slip. For the gross sliding, a large number of oxygen atoms should be observed across the whole contact zone.

To perform the EDS, the specimens were taken to a Scanning Electron Microscope (SEM) to evaluate the quantity and distribution of aluminum and oxygen particles on the contact zone. Results for one of the fretting tests (specimen no. 2) are presented in a color mapping form in Fig. 2.13 and for all specimens in Appendix A. The blue and green colors indicate the presence of oxygen and aluminum particles, respectively. For all tests, it can be observed that oxygen particles are concentrated at the edges of the contact mark. These results demonstrate that the wire-wire fatigue tests presented typical characteristics of fretting in the partial slip regime, where  $Al_2O_3$  particles were possibly formed at the micro-slip zones. Note that Rocha (2019) performed fatigue tests on an AAAC 900 MCM conductor and also observed the development of partial slip fretting regime on the AA6201-T81 wires located at the critical region of the conductor (close to the suspension clamp). This result indicates that it is possible to reproduce the fretting regime observed in wires of a conductor using the four-actuator fretting fatigue apparatus developed at the University of Brasilia.

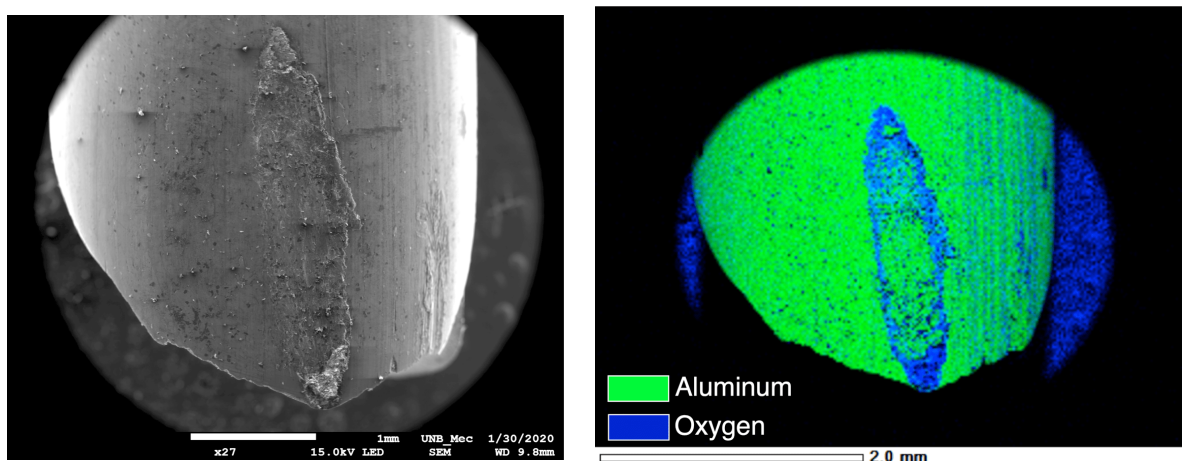


Figure 2.13: EDS of specimen no. 2 showing the presence of oxygen (blue) and aluminum (green) particles.



## 2.5.2 Fracture surface examination

The EDS analysis described in Section 2.5.1 showed that, for all fretting tests, the contact marks exhibited typical characteristics of partial slip fretting regime. This section presents the macro- and micro-fractographic observations that were conducted to verify if the cracks initiated due to fretting at the contact marks.

To perform the fractography, the upper portions of the broken specimens were observed in a Scanning Electron Microscope. The reason for observing only the upper part of the specimen was that most of the contact mark remains at this portion of the wire specimen. Figure 2.14 shows the fracture surface of the specimen no. 2 (refer to Table 2.1 for the loading conditions). It can be observed that a slightly smoother and darker region (I) is formed centered at the contact mark while a lighter and rougher region (II) is formed at the rest of the surface.

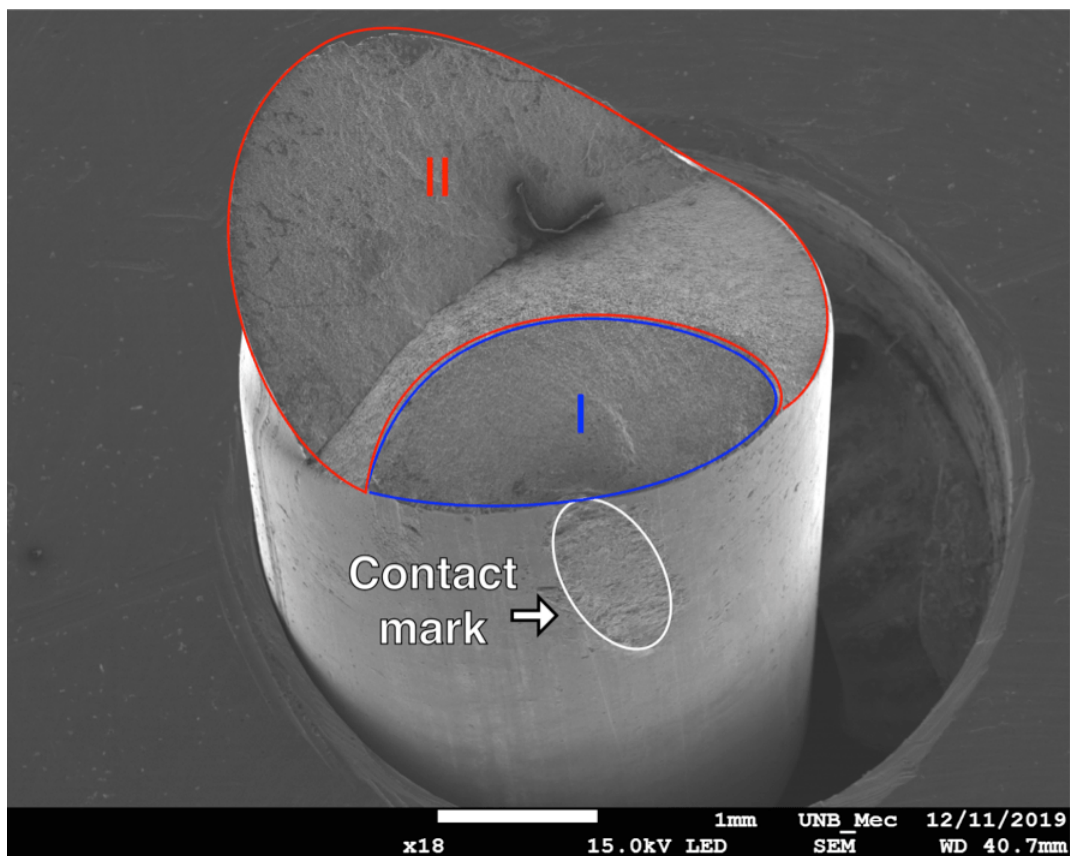


Figure 2.14: Fracture surface of the specimen no. 2.

Details of both regions are shown in Fig. 2.15. For region I, striation marks were found near the contact mark. Such features indicate crack propagation due to fatigue loading. Besides, the striations tend to be concentric with the origin of the failure, which reinforces the idea that the crack initiated from the contact mark. As for the rest of the surface, dimples were found scattered throughout region II. These features are characterized by the formation of a set of microcavities and indicate the occurrence of ductile fracture in the region of final fracture. Hence, it was concluded that the crack initiated at the contact mark, propagated due to the

fatigue loading in region I and caused a final ductile fracture at the rest of the surface (region II). Although the presence of dimples and striation marks was not investigated in all specimens, all fractured surfaces exhibited similar characteristics, with the formation of a smoother region around the contact mark and a rougher region for the rest of surface. Such results suggest that in all tests, cracks initiated at the contact marks, but further investigations would be desirable to ascertain the source of failures in all specimens.

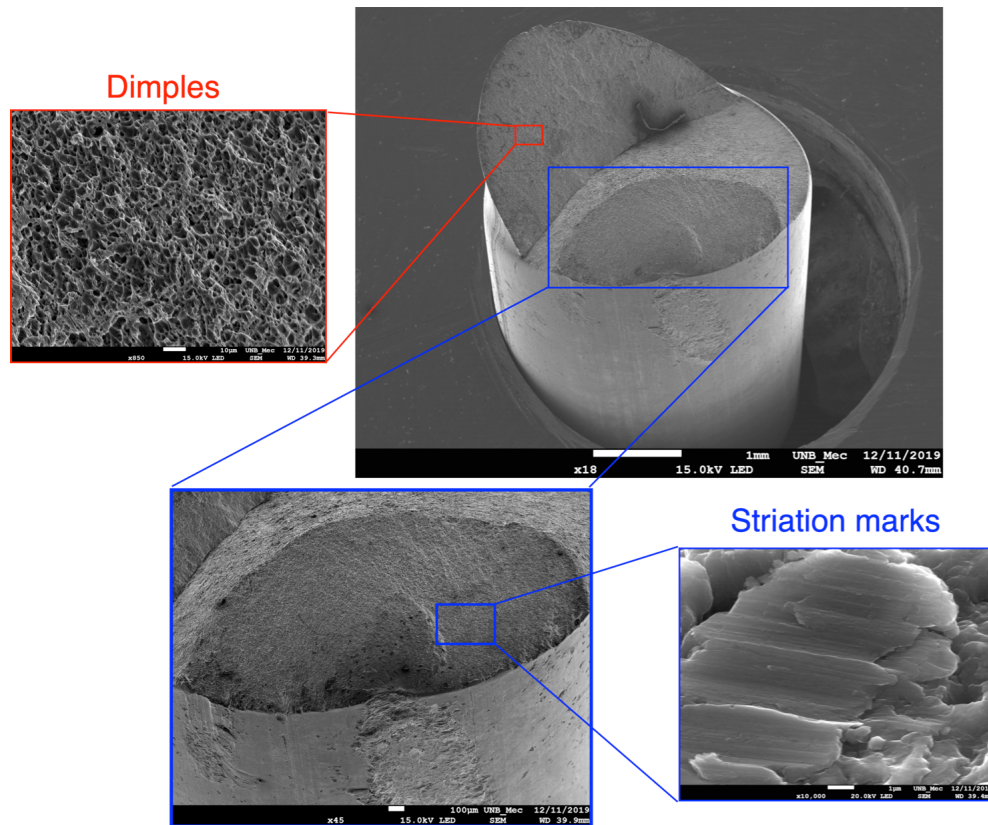


Figure 2.15: Details of the striation marks and dimples found at the fracture surface of the specimen no. 2.

### 2.5.3 Comparison of observed and estimated critical plane orientations

A critical plane approach should be able to predict fatigue life well for a variety of loading conditions and also be consistent with the physically observed damage (Socie and Bannantine, 1988; Jiang et al., 2007), i.e., the critical plane where a crack is formed. In this section, the non-local SWT fatigue criterion described in Section 2.3 is evaluated with respect to its capability to describe the crack orientations observed in the AA6201-T81 wires. To describe this plane, two angles  $\theta$  and  $\phi$  are used, where the former represents the orientation of the surface crack, and the latter represents the inclination of the crack.

Fig. 2.16 exemplifies the measurement of angles  $\theta$  and  $\phi$  for specimen no. 2 using a Scanning Electron Microscope. The measured angles for all broken wires are presented in Appendix B. The angles  $\theta$  and  $\phi$  were estimated by the fatigue model using cyclic stresses



outputted by the linear elastic and the elastic-perfectly plastic contact models of the wires. The observed and estimated angles are summarized in Table 2.2, where the subscript “obs” refers to the experimental observations, while “est, LE” and “est, EP” refer to angles estimated by the fatigue model using the linear elastic and the elastic-plastic material behaviors, respectively.

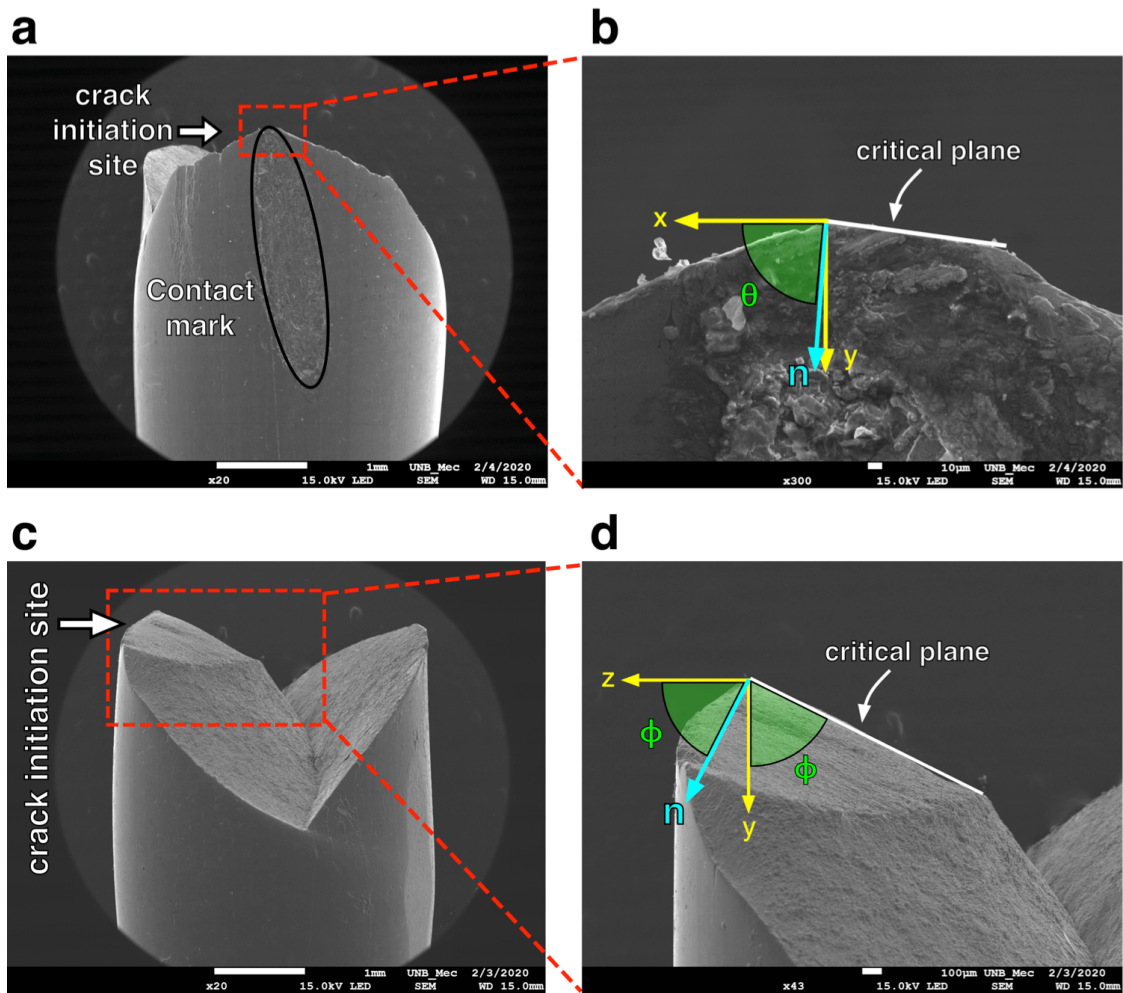


Figure 2.16: Schematic of the procedure to measure the critical plane orientation of the specimen no. 2

Table 2.2: Comparison between observed and estimated critical plane orientations.

Specimen ID	$\theta_{\text{obs}}$ [°]	$\theta_{\text{est, LE}}$ [°]	$\theta_{\text{est, EP}}$ [°]	$\phi_{\text{obs}}$ [°]	$\phi_{\text{est, LE}}$ [°]	$\phi_{\text{est, EP}}$ [°]
01	96	85	90	65	80	80
08	91	90	90	62	80	80
24	89	90	90	66	80	80
23	90	85	90	70	80	80
02	85	85	90	63	80	80
11	99	90	90	52	80	80
17	86	90	90	81	85	80
06	94	90	90	67	85	80
10	96	90	90	60	85	80

The results presented in Table 2.2 show that the critical plane SWT fatigue model was capable of predicting the crack initiation plane with reasonable accuracy. No significant difference was observed between the predictions obtained using a linear elastic or an elastic-perfectly plastic contact models. It is also worth noticing that there was little variation of the observed and predicted critical plane orientations among all tests

While the early crack orientation presents little variation among the wire specimens, two distinct behaviors were observed for the final fracture surface: V-type and 45°-type of fractures. An example of each of the fracture types is presented in Fig. 2.17. The V-type and 45°-type of fractures were previously observed in tests with conductor-clamp assemblies, including tests with the AAAC 900 MCM conductor (Kalombo, 2017; Fadel et al., 2012; Azevedo et al., 2009). The majority of the broken specimens (78%) presented the V-type of fracture while only two (22%) presented the 45°-type of fracture. It is worth highlighting that these two specimens were used in tests with the same loading conditions (compressive force of 750 N, mean load of 3150 N and force amplitude of 292 N). This suggests that the final fracture surface of the AA6201-T81 wires may be affected by the loading conditions.

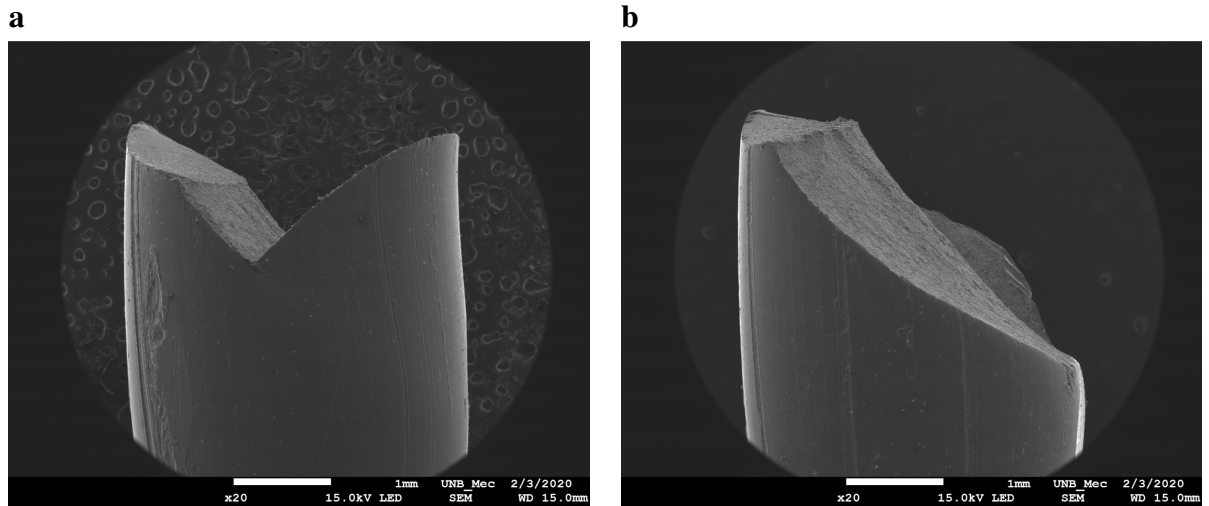


Figure 2.17: Final fracture surfaces observed on the wire specimens: (a) V-type of fracture in specimen no. 8 and (b) 45°-type of fracture in specimen no. 17

## 2.5.4 Comparison of observed and estimated lives

As a first step towards the application of the life estimation methodology for wire-wire contact problems, the constants of the fatigue model have to be determined. The fatigue model was calibrated using the fatigue test data from the plain and V-notched specimens shown in Fig. 2.3. The constants of the SWT vs.  $N_f$  relation, Eq. (2.4), were determined by best fitting the test data from plain wires subjected to fully reversed axial loading. This procedure yielded the following expression:

$$\text{SWT} = 252N_f^{-0.03} \quad (2.5)$$

The relation between the characteristic length,  $L$ , and the number of cycles to failure,  $N_f$ , was obtained using the test data from the V-notched specimens subjected to fully reversed axial loading. Following the procedure described in Section 2.3,  $L$ - $N_f$  data points were first obtained and then fitted by the following power-law relation:

$$L = 1765N_f^{-0.24} \mu\text{m} \quad (2.6)$$

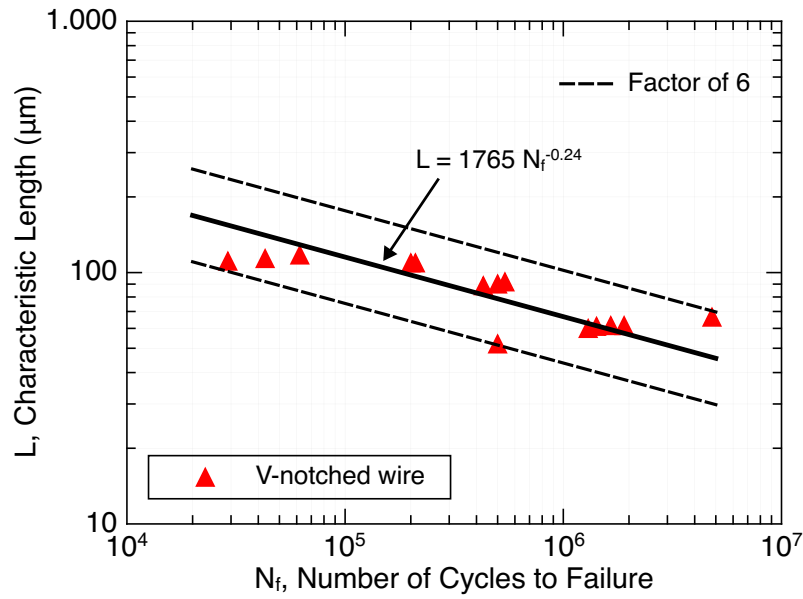


Figure 2.18: Correlation between the characteristic length and the number of cycles to failure of the V-notched wires.

The comparison between the number of cycles to failure observed in the wire-wire fatigue tests and the estimates made by the nonlocal SWT fatigue model is shown in Fig. 2.19. The solid diagonal line signifies a perfect correlation between predicted and observed lives, and the dashed lines represent factor-of-five boundaries. Predictions considering a linear elastic material behavior (represented by open symbols) were overly conservative. This result was not expected since the use of a linear elastic material model provided reasonable life predictions of AA1350-H19 wire-wire fatigue tests conducted in an earlier study (Rocha et al., 2019). In an attempt to improve the agreement with experimental data, new simulations were conducted using an elastic-perfectly plastic material behavior. Most fatigue life estimates from these new simulations (represented by solid symbols) were within the factor-of-five boundaries, which means a significant improvement relative to the life estimates made with the linear elastic material model.

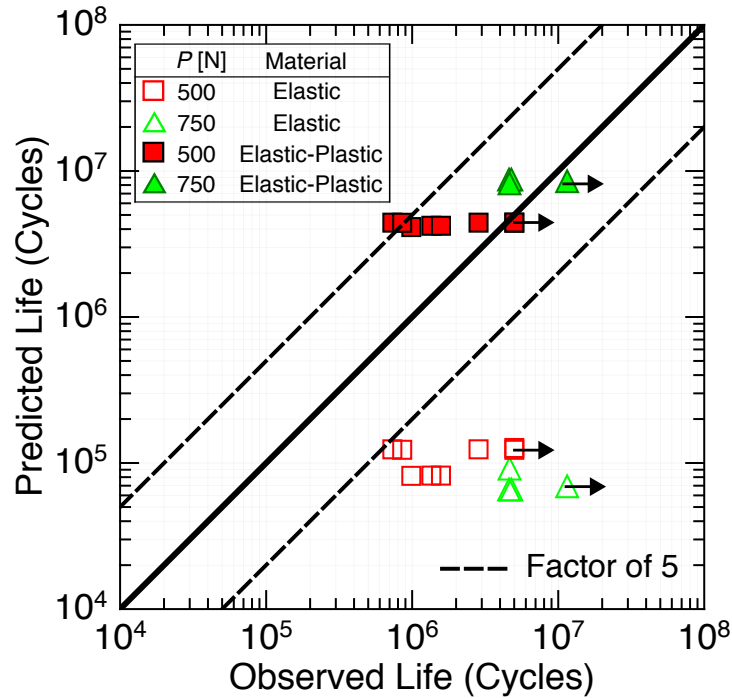


Figure 2.19: Observed lives of the wire-wire fatigue tests vs. estimates using the nonlocal SWT fatigue criterion.

Fig. 2.19 shows that the life estimates made by combining an elastic-perfectly plastic material model with the SWT fatigue criterion are sensitive to the normal force applied to the wire-wire test configuration. Higher fatigue lives were predicted for the tests with a normal load of 750 N than for the tests with 500 N. However, the effect of mean force on fatigue life was not appropriately described by the model since, for the tests conducted under a normal force of 500 N, all simulations provided almost identical fatigue life estimates.

### 2.5.5 Comparison of observed and estimated contact marks

In the FE-based simulations of the contact of wires using the elastic-perfectly plastic material model, elliptical contact marks are produced due to the plastic deformation in the contact zone. To evaluate the quality of the wire-wire contact simulations, the dimensions of the contact marks estimated by the elastic-plastic FE model were compared to the dimensions observed in the fretting tests.

Fig. 2.20 gives an example of observed and estimated contact marks for the specimen no. 2. The results for the other specimens are reported in Appendix C. The observed lengths of the major and minor axes of the elliptical contact mark ( $2a_{obs}$  and  $2b_{obs}$ , respectively) were measured using a confocal laser microscope. To numerically estimate the lengths of the major and minor axes ( $2a_{est}$  and  $2b_{est}$ , respectively), the output variable CSTATUS was selected in Abaqus/CAE to visualize the nodes in the contact zone under stick or slip condition. The relative percentage difference between the observed and estimated dimensions were calculated and denoted by  $I_{2a}$  for the major axis and  $I_{2b}$  for the minor axis. It should be noted that attempts to measure

the depth of the contact mark were also performed, but the results obtained were inconclusive possibly because of the minute indentation caused by the applied normal forces.

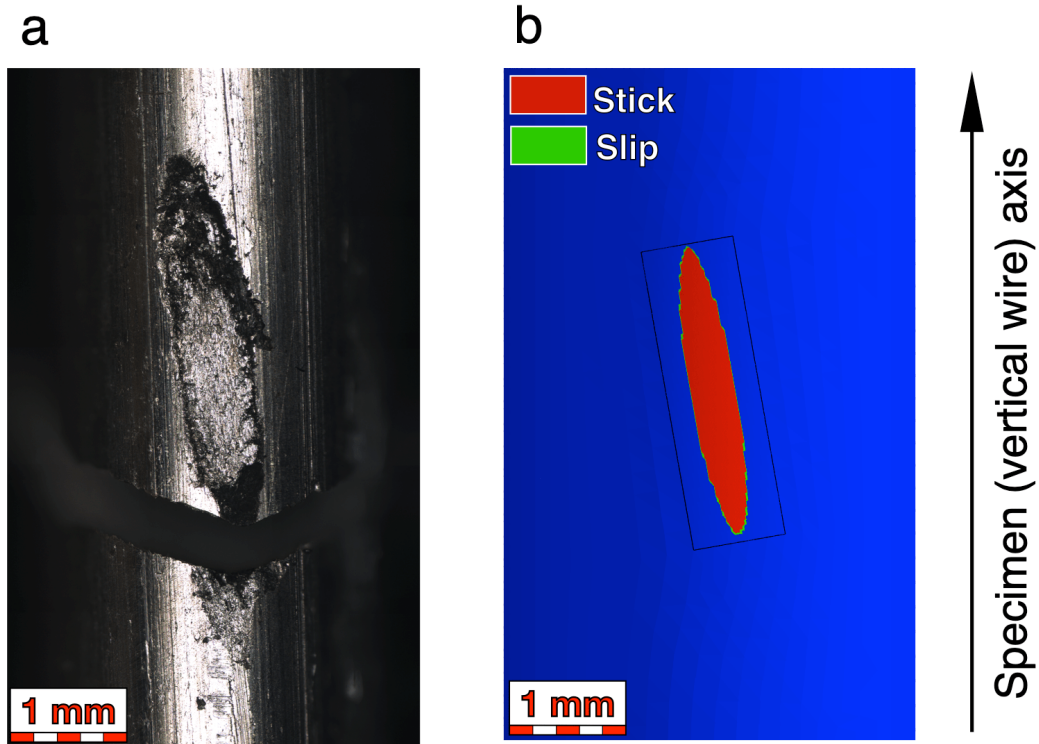


Figure 2.20: Comparison between the (a) observed and (b) estimated contact marks for the specimen no. 2.

Table 2.3: Observed and estimated dimensions of the contact marks.

Specimen ID	$2a_{\text{obs}}$ [ $\mu\text{m}$ ]	$2a_{\text{est}}$ [ $\mu\text{m}$ ]	$2b_{\text{obs}}$ [ $\mu\text{m}$ ]	$2b_{\text{est}}$ [ $\mu\text{m}$ ]	$I_{2a}$ [%]	$I_{2b}$ [%]
01	3816	2370	612	378	-38	-38
08	3650	2521	582	418	-31	-28
24	2871	2521	614	418	-12	-32
23	3202	2526	627	366	-21	-42
02	3376	2526	704	366	-25	-48
11	2936	2521	737	402	-14	-45
26	3780	2521	720	402	-33	-44
04	3372	2500	655	376	-26	-43
17	4080	2982	660	514	-27	-22
06	4538	2982	648	514	-34	-21
18	4024	2982	687	514	-26	-25
10	3723	2967	733	514	-20	-30

Table 2.3 summarizes the observed and estimated dimensions of the contact marks. For the tests with a normal force of 500 N, the relative differences between the estimated and observed lengths of the major axes ( $I_{2a}$ ) were within a range of -38% to -12%, and in a range of -48% to -28% for the minor axes ( $I_{2b}$ ). Similarly, For the tests with a normal force of 750 N, the differences were in a range of -34% to -20% for the major axes, and in a range of -30% to -21% for the minor axes. Note that the negative differences obtained for the dimensions of all contact marks indicate that the predictions are undersized compared to the marks observed in the fretting tests. These results show that the elastic-plastic contact model was capable of estimating the dimensions of the contact marks with reasonable accuracy, which is remarkable considering that the effect of wear was not taken into account, and that the cyclic stress-strain behavior of the material was calibrated using test data from a monotonic tension test.

### 3 Conclusions

Fretting fatigue tests have been performed on 6201-T81 aluminum alloy wires crossed at an angle of  $20^\circ$ . A nonlocal Smith–Watson–Topper fatigue criterion was evaluated with respect to its capability to predict the observed fatigue lives and critical planes orientations. The capability of the elastic-plastic contact model to estimate the size of the contact marks was also evaluated. The main findings are summarized as follows:

For the fretting fatigue behavior of the AA6201-T81 wires:

- (1) The fatigue life of the wires can be affected by the presence of a mean force. For the tests performed with a normal force of 500 N, it was observed that lower mean forces resulted in longer fatigue lives. However, no clear correlation was observed between mean force and fatigue life for the tests with a normal force of 750 N.
- (2) The normal force was observed to have a significant effect on fatigue life. For instance, for the fatigue tests performed with axial force amplitude of 292 N and mean axial force of 3150 N, the lives of the specimens subjected to a normal force of 750 N were about five times higher than the life of the specimen under a normal force of 500 N.
- (3) All wire-wire tests presented characteristics of partial slip fretting regime, with distinguishable stick and slip zones. Rocha (2019) performed fatigue tests on an AAAC 900 MCM conductor and also observed the development of partial slip fretting regime on the AA6201-T81 wires located at the critical region of the conductor (close to the suspension clamp). This result indicates that it is possible to reproduce the loading conditions and fretting regime observed in wires of a conductor using the four-actuator fretting fatigue apparatus developed at the University of Brasilia.
- (4) The examination of the striation marks and dimples at the fracture surfaces of the wire specimens indicated that crack initiation occurred at the extremity of the major axis of the elliptical contact mark, propagated due to fatigue loading and caused final fracture of the wire. Although the presence of striation marks and dimples was not investigated in all specimens, similarities between the fracture surfaces suggest that, in all specimens, cracks initiated at the extremity of the major axes of the contact marks.
- (5) Two distinct fracture surfaces were identified in the broken wires: V-type and a  $45^\circ$ -type of fractures. The majority of the wire specimens presented the V-type of fracture. Two specimens tested under the same loading conditions exhibited a  $45^\circ$ -type of fracture. This suggests that the final fracture behavior of the wire depends on the loading conditions.



For the fatigue model and the elastic-plastic contact model:

- (6) Fatigue lives estimated using the cyclic stresses outputted from a linear elastic contact model of wires were overly conservative. The use of an elastic-perfectly plastic material behavior in the contact model significantly improved life prediction, with most of the estimated lives falling within factors of five of the observed lives.
- (7) The life estimates using the elastic-perfectly plastic contact model combined with the nonlocal SWT fatigue criterion were sensitive to the applied normal force: for a normal force of 750 N, the estimated lives were about two times longer than those for a normal force of 500 N.
- (8) The mean force effect on the fatigue life of a wire was not well described by the life prediction methodology. For the tests conducted under a normal load of 500 N, all simulations provided almost identical fatigue lives. Further improvement of the methodology is required to better take into account this effect.
- (9) The major and minor axes of the contact marks simulated using the elastic-perfectly plastic contact model were within -48% to -12% of the observed values.
- (10) The Smith–Watson–Topper fatigue criterion with a critical plane interpretation was capable of describing the early crack orientations observed in the wire specimens with reasonable accuracy.

# References

- Adriano V. S. R., Martínez J. M. G., Ferreira J. L. A., Araújo J. A., da Silva C. R. M., 2018. The influence of the fatigue process zone size on fatigue life estimations performed on aluminum wires containing geometric discontinuities using the Theory of Critical Distances. *Theoretical and Applied Fracture Mechanics*, Vol. 97, pp. 265-278.
- Aggarwal R. K., Johns A. T., Jayasinghe J. A. S. B., Su W., 2000. An overview of the condition monitoring of overhead lines. *Electric Power Systems Research*, Vol. 53, pp. 15-22.
- Araújo J. A., Castro F. C., Matos I. M., Cardoso R. A., 2020. Life prediction in multiaxial high cycle fretting fatigue. *International Journal of Fatigue*, Vol. 134, pp. 105504.
- Azevedo C. R. F., Cescon T., 2002. Failure analysis of aluminum cable steel reinforced (ACSR) conductor of the transmission line crossing the Paraná River. *Engineering Failure Analysis*, Vol. 9, pp. 645-664.
- Azevedo C. R. F., Henriques A. M. D., Pulino Filho A. R., Ferreira J. L. A., Araújo J. A., 2009. Fretting fatigue in overhead conductors: Rig design and failure analysis of a Grosbeak aluminium cable steel reinforced conductor. *Engineering Failure Analysis*, Vol. 16, pp. 136-151.
- Barber K. W., Callaghan K. J., 1995. Improved overhead conductors using aluminium alloy 1120. *IEEE Transactions on Power Delivery*, Vol. 10(1), pp. 403-409.
- Cardou A., Cloutier L., Lanteigne J., M'Boup P., 1990. Fatigue Strength Characterization of ACSR Electrical Conductors at Suspension Clamps. *Electric Power Systems Research*, Vol. 19, pp. 61-71.
- Chen G., Wang X., Wang J., Liu J., Zhang T., Tang W., 2012. Damage investigation of the aged aluminium cable steel reinforced (ACSR) conductors in a high-voltage transmission line. *Engineering Failure Analysis*, Vol. 19, pp. 13-21.
- Díaz, J. I. M., 2018. Avaliação do efeito do fretting sobre o comportamento da liga de alumínio Al 1350-H19. University of Brasilia, M.Sc Dissertation.
- Dowling N. E., Calhoun C. A., Arcari A., 2009. Mean stress effects in stress-life fatigue and the Walker equation. *Fatigue and Fracture of Engineering Materials and Structures*, Vol. 32, pp. 163-179.
- Fadel A. A., Rosa D., Murça L. B., Ferreira J. L. A., Araújo J. A., 2012. *International Journal*

of Fatigue, Vol. 42, pp. 24-34.

Fatemi A., Shamsaei N., 2011. Multiaxial fatigue: An overview and some approximation models for life estimation. *International Journal of Fatigue*, Vol. 33, pp. 948-958.

Fricke W. G., Rawlins C. B., 1968. Importance of fretting in vibration failures of stranded conductors. *IEEE Transactions on Power Apparatus and Systems*, Vol. PAS-87 (6), pp. 1381-1384.

Garcia M. A., 2019. Concepção, fabricação e avaliação de um dispositivo de fadiga por fretting em fios de alumínio de cabos condutores. University of Brasilia, M.Sc Dissertation.

Greenfield E. W., 1959. High-strength aluminum alloy conductors. *Transactions of the American Institute of Electrical Engineers. Part III: Power Apparatus and Systems*, Vol. 78(4), pp. 1449-1455.

Guimarães P. G., Miller M. D., 2012. Brazilian transmission system: A race for the future. *Electrical Transmission and Substation Structures*, pp. 401-415.

Hazan E., 1970. Arc-fault characteristics of bare overhead distribution conductors: Seven-strand AAAC (6201) and 6/1 ACSR. *IEEE Transactions on Power Apparatus and Systems*, Vol. PAS-89 (3), pp. 411-420.

Hills D. A., Nowell D., 1994. *Mechanics of fretting fatigue*. Springer Science & Business Media.

IEEE, 2015. An introductory discussion on aeolian vibration of single conductors. *Transmission & Distribution Comitee, Technical Report PES-TR17*.

Jiang Y., Hertel O., Vormwald M., 2007. An experimental evaluation of three critical plane multiaxial fatigue criteria. *International Journal of Fatigue*, Vol. 29, pp. 1490-1502.

Kalombo R. B., 2017. Evaluation of the fatigue resistance of power line conductors function of the H/w parameter. University of Brasilia, Doctoral thesis.

Kalombo R. B., Araújo, J. A., Ferreira, J. L. A., da Silva, C. R. M., Alencar R., Capra A. R., 2015. Assessment of the fatigue failure of an All Aluminum Alloy Cable (AAAC) for a 230 kV transmission line in the Center-West of Brazil. *Engineering Failure Analysis*, Vol. 61, pp. 77-87.

Karabay S., 2006. Modification of AA-6201 alloy for manufacturing of high conductivity and extra high conductivity wires with property of high tensile stress after artificial aging heat treatment for all-aluminium alloy conductors. *Materials and Design*, Vol. 27, pp. 821-832.

Lévesque F., Goudreau S., Cloutier L., 2011. Elastic-plastic microcontact model for elliptical contact areas and its application to a treillis point in overhead electrical conductors. *Journal of*

Tribology, Vol. 133, pp. 011401-1.

Ma X., Gao L., Zhang J., Zhang L., 2017. Fretting wear behaviors of Aluminum Cable Steel Reinforced (ACSR) conductors in high-voltage transmission line. *Metals*, Vol. 7(9), pp. 373.

Matos I. M., Rocha P. H. C., Araújo J. A., Castro F. C., 2019. Fatigue life prediction of AA1350-H19 wire under high stress gradient. *Proceedings of the 7th International Symposium on Solid Mechanics - MECSOL 2019*.

McGill P. B., Ramey G. E., 1986. *J. Energy Eng.*, Vol. 112 (3), pp.168-184.

Neuber H., 1958. *Theory of notch stresses: Principles for exact calculation of strength with reference to structural form and material*. Berlin: Springer.

Ouaki B., Goudreau S., Cardou A., Fiset M., 2003. Fretting fatigue analysis of aluminium conductor wires near the suspension clamp: metallurgical and fracture mechanics analysis. *J Strain Analysis*, Vol. 38, pp. 133-147.

Peterson R. E., 1959. Notch sensitivity. *Metal Fatigue*, pp. 293-306.

Rhaiem E., Bouraoui T., Elhalouani F., 2010. Anticorrosive solution of 6201 aluminum alloy used in STEG company's overhead transmission lines. *IOP Conference Series: Materials Science and Engineering*, Vol. 13, pp. 012038.

Rocha P. H. C., 2019. *Studies of fatigue on two contacting wires of overhead conductors: Experiments and modeling*. University of Brasilia, M.Sc Dissertation.

Rocha P. H. C., Díaz J. I. M., da Silva C. R. M., Araújo J. A., Castro F. C., 2019. Fatigue of two contacting wires of the ACSR Ibis 397.5 MCM conductor: Experiments and life prediction. *International Journal of Fatigue*, Vol. 127, pp. 25-35.

Said J., Garcin S., Fouvry S., Cailletaud G., Yang C., Hafid F., 2020. A multi-scale strategy to predict fretting-fatigue endurance of overhead conductors. *Tribology International*, Vol. 143, pp. 106053.

Smith K. N., Watson P., Topper T. H., 1970. A stress-strain function for the fatigue of metals. *Journal of Materials*, Vol. 5(4), pp. 767-778.

Socie D., 1987. Multiaxial fatigue damage models. *J. Eng. Mater. Technol.*, Vol. 109(4), pp. 293-298.

Socie D., Bannantine J., 1988. Bulk deformation fatigue damage models. *Materials Science and Engineering*, Vol. A103, pp. 3-13.

Susmel L., Taylor D., 2007. A novel formulation of the Theory of Critical Distances to estimate lifetime of notched components in the medium-cycle fatigue regime. *Fatigue Fract Engng Mater Struct*, Vol. 30, pp. 567-581.

Taylor D., 1999. Geometrical effects in fatigue: A unifying theoretical model *International Journal of Fatigue*, Vol. 21, pp. 413-420.

Wikimedia Commons, 2013. Transmission tower Long Bennington. Available at: [https://commons.wikimedia.org/wiki/File:2013\\_Transmission\\_tower\\_Long\\_Bennington.jpg](https://commons.wikimedia.org/wiki/File:2013_Transmission_tower_Long_Bennington.jpg)

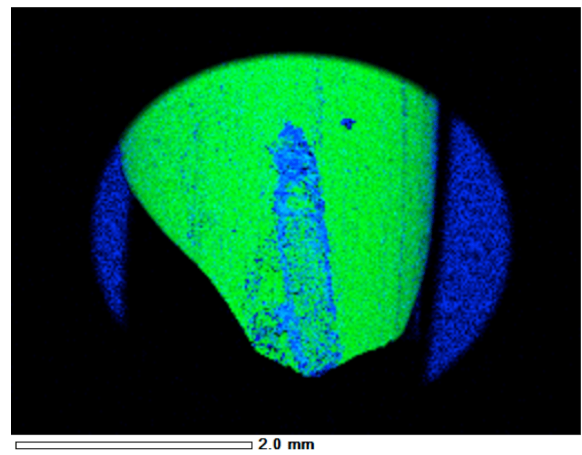
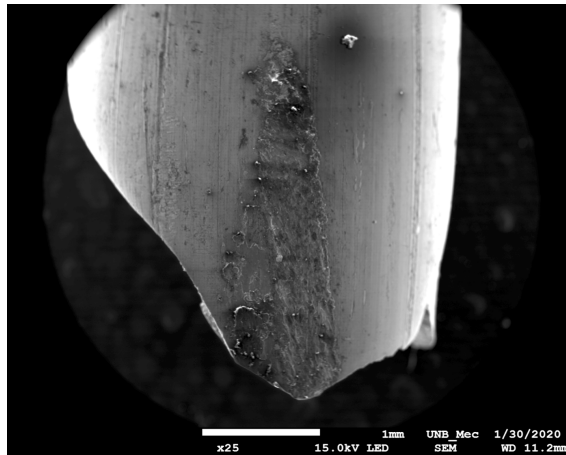
Zhao M., Zhou Q., Zhao X., 2011. The Fretting Fatigue Analysis between Strands of ACSR. *International Conference on Electrical and Control Engineering*, pp. 3240-3242.

Zhou Z. R., Cardou A., Fiset M., Goudreau S., 1994. Fretting fatigue in electrical transmission lines. *Wear*, Vol. 173, pp. 179-188.

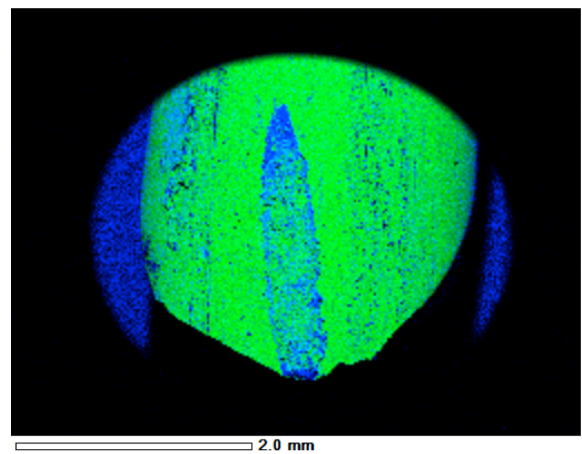
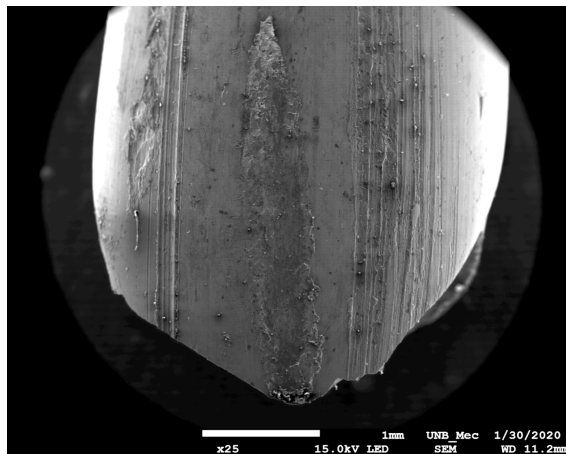
# Appendices

# A Energy-dispersive spectroscopy mapping of the contact marks

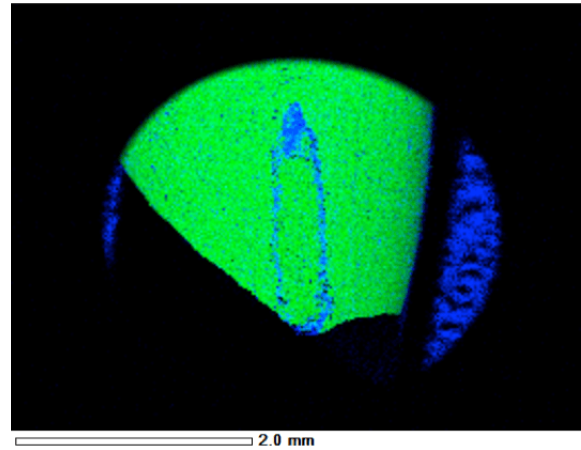
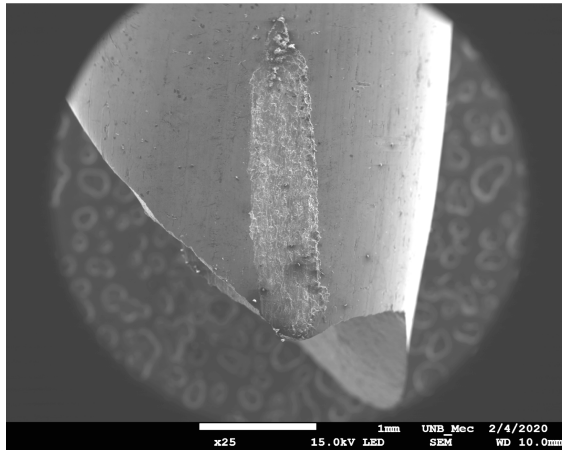
Specimen 01 ( $P = 500$  N,  $F_m = 3150$  N,  $N_f = 985,499$  cycles)



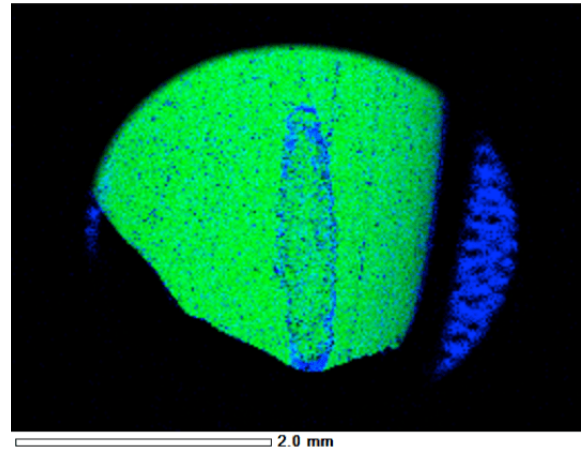
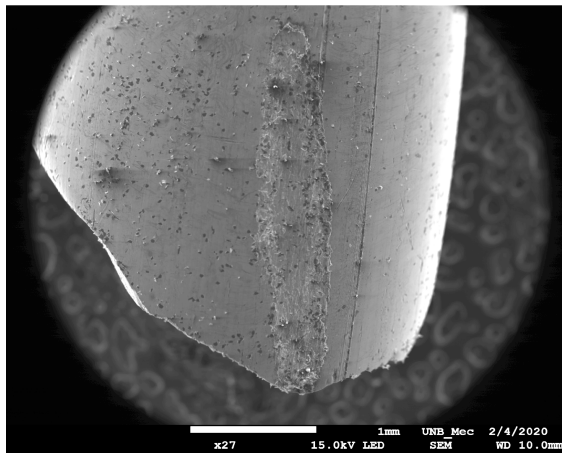
Specimen 08 ( $P = 500$  N,  $F_m = 2990$  N,  $N_f = 1,350,201$  cycles)



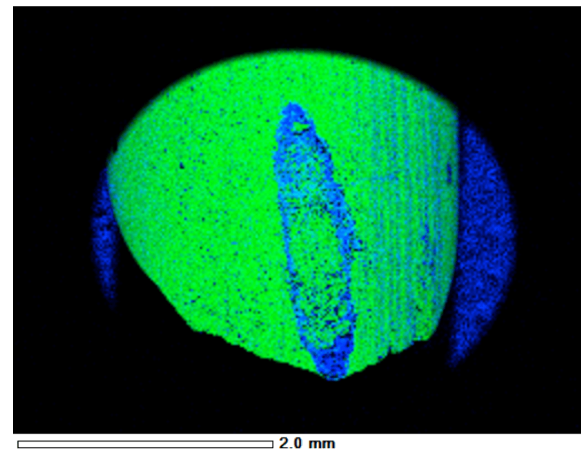
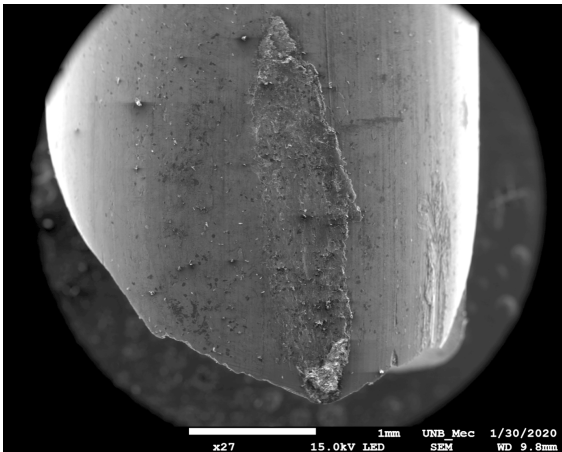
Specimen 24 ( $P = 500$  N,  $F_m = 2990$  N,  $N_f = 1,572,473$  cycles)



Specimen 23 ( $P = 500$  N,  $F_m = 2800$  N,  $N_f = 730,520$  cycles)

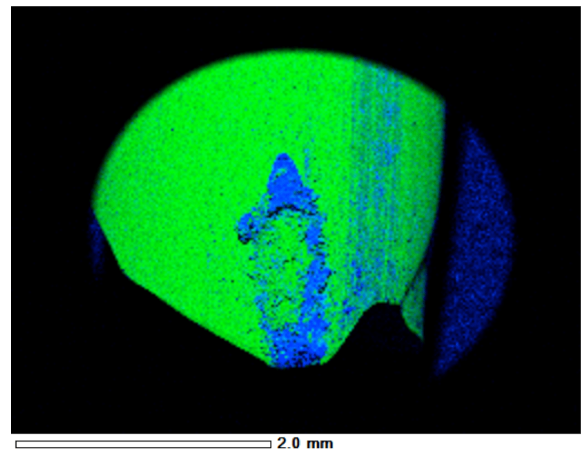
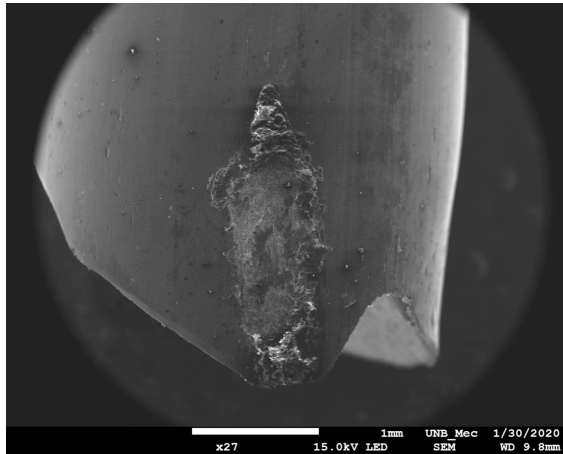


Specimen 02 ( $P = 500$  N,  $F_m = 2800$  N,  $N_f = 2,844,101$  cycles)

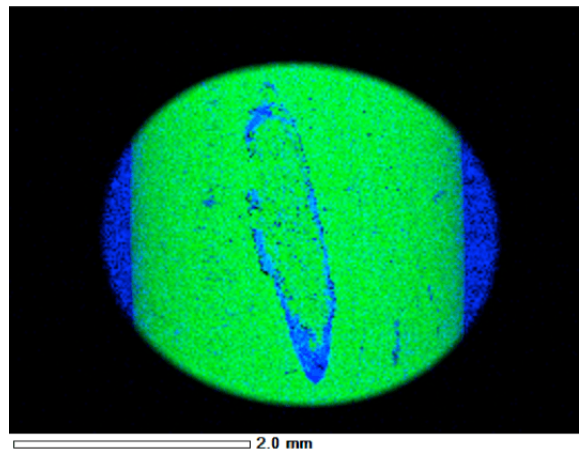
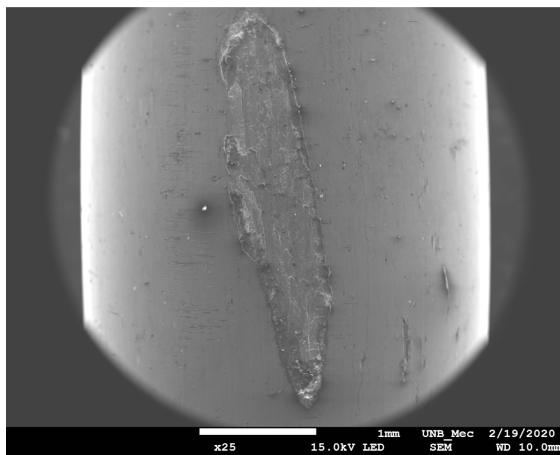




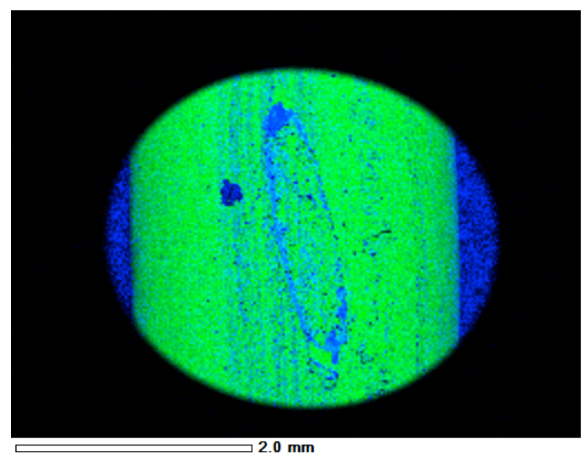
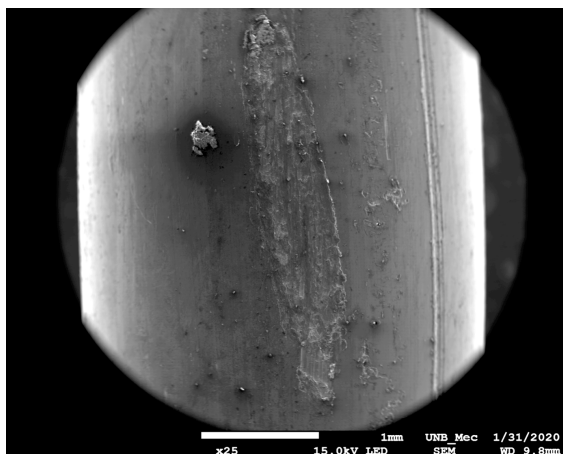
Specimen 11 ( $P = 500 \text{ N}$ ,  $F_m = 2600 \text{ N}$ ,  $N_f = 853,072 \text{ cycles}$ )



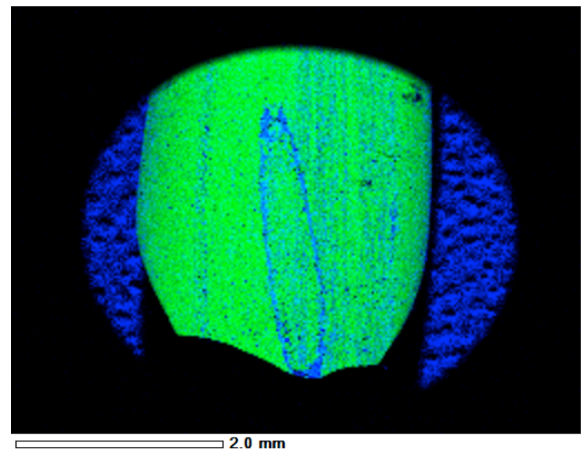
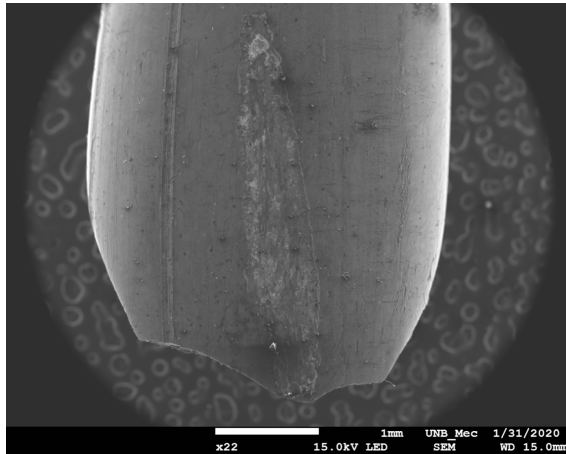
Specimen 25 ( $P = 500 \text{ N}$ ,  $F_m = 2600 \text{ N}$ ,  $N_f > 5,000,000 \text{ cycles}$ )



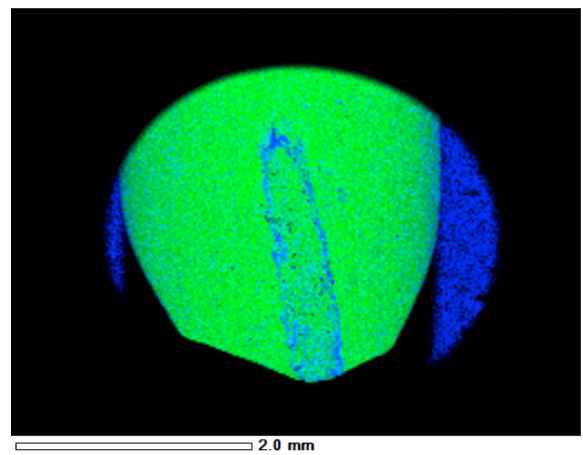
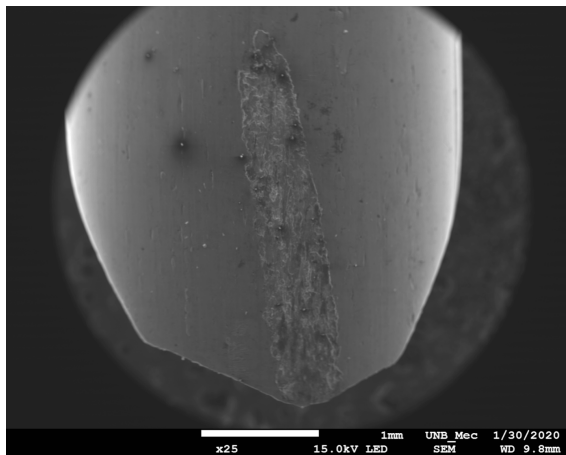
Specimen 04 ( $P = 500 \text{ N}$ ,  $F_m = 2490 \text{ N}$ ,  $N_f > 5,000,000 \text{ cycles}$ )



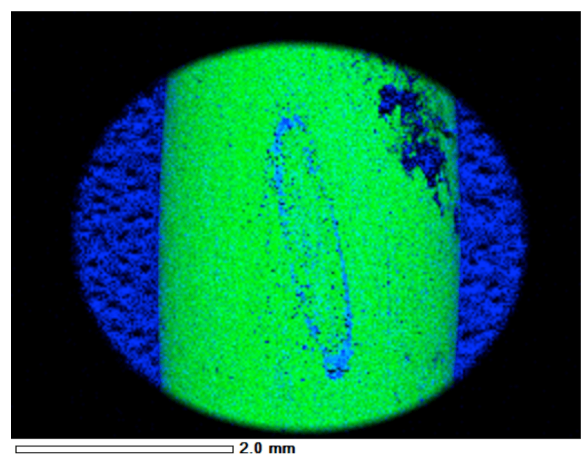
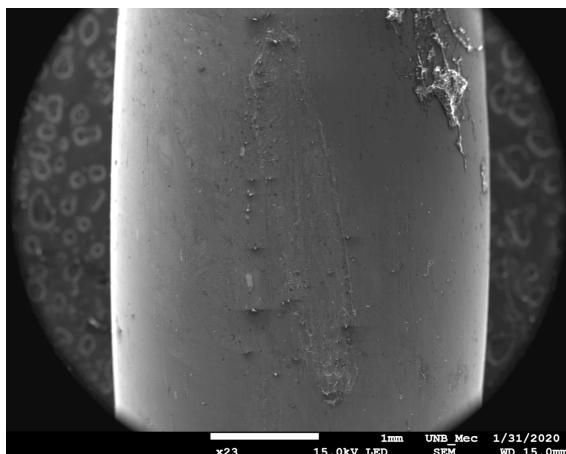
Specimen 17 ( $P = 750 \text{ N}$ ,  $F_m = 3150 \text{ N}$ ,  $N_f = 4,610,117$  cycles)



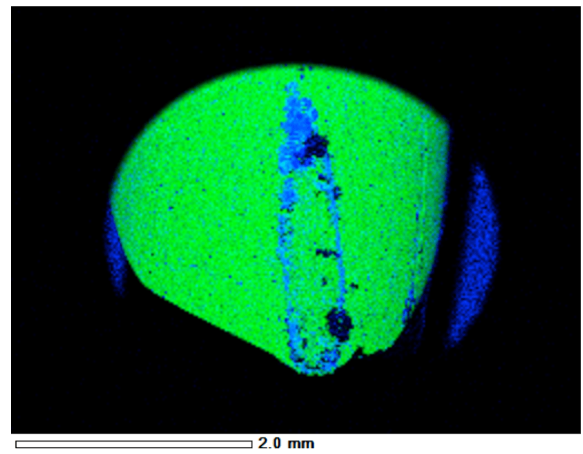
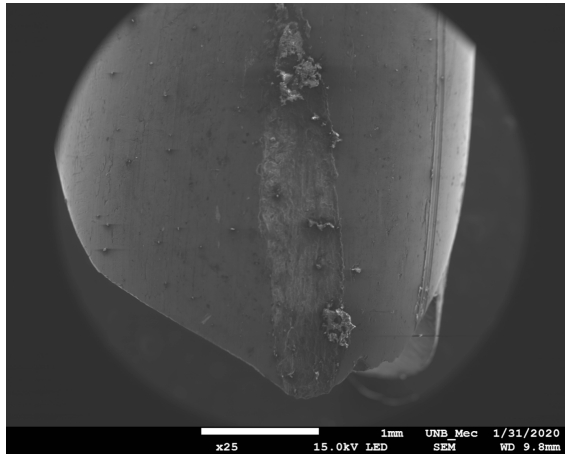
Specimen 06 ( $P = 750 \text{ N}$ ,  $F_m = 3150 \text{ N}$ ,  $N_f = 4,773,894$  cycles)



Specimen 18 ( $P = 750 \text{ N}$ ,  $F_m = 2990 \text{ N}$ ,  $N_f > 11,513,988$  cycles)

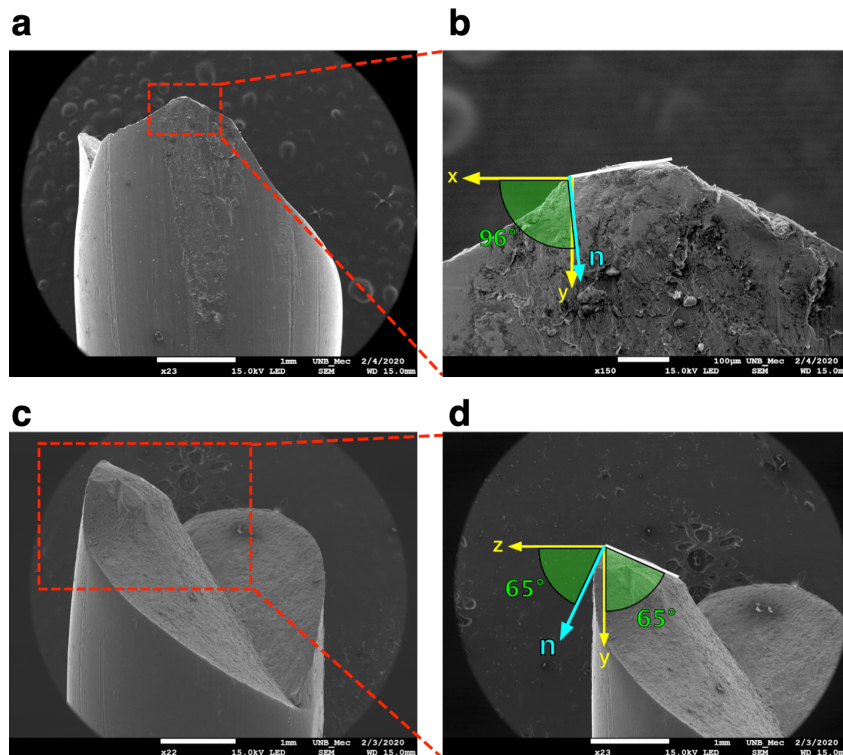


Specimen 10 ( $P = 750$  N,  $F_m = 2800$  N,  $N_f = 4,640,891$  cycles)



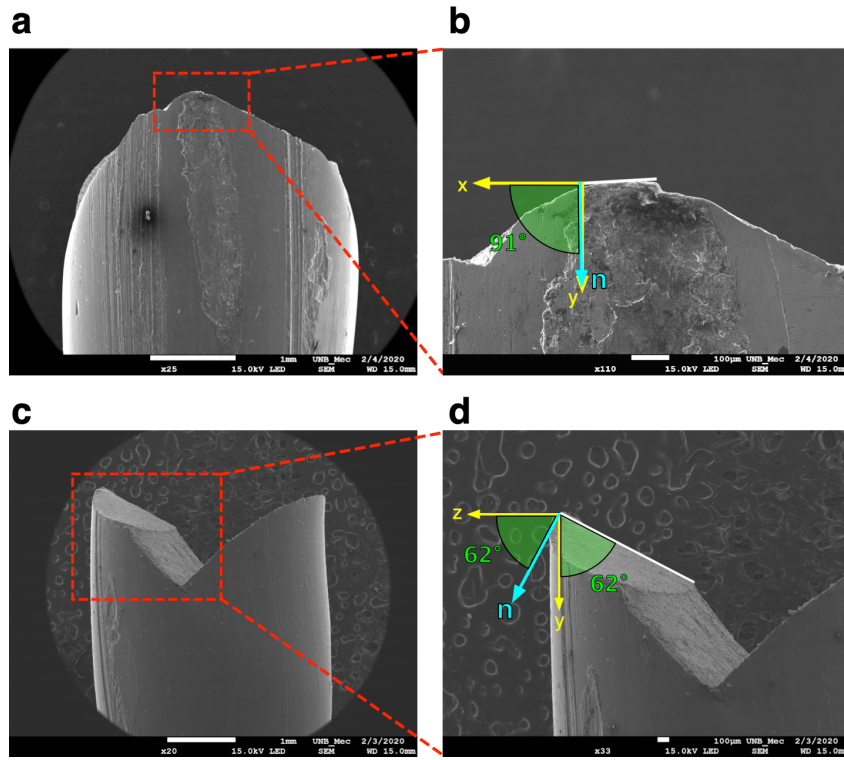
## B Observed critical planes

Specimen 01 ( $P = 500$  N,  $F_m = 3150$  N,  $N_f = 985,499$  cycles)

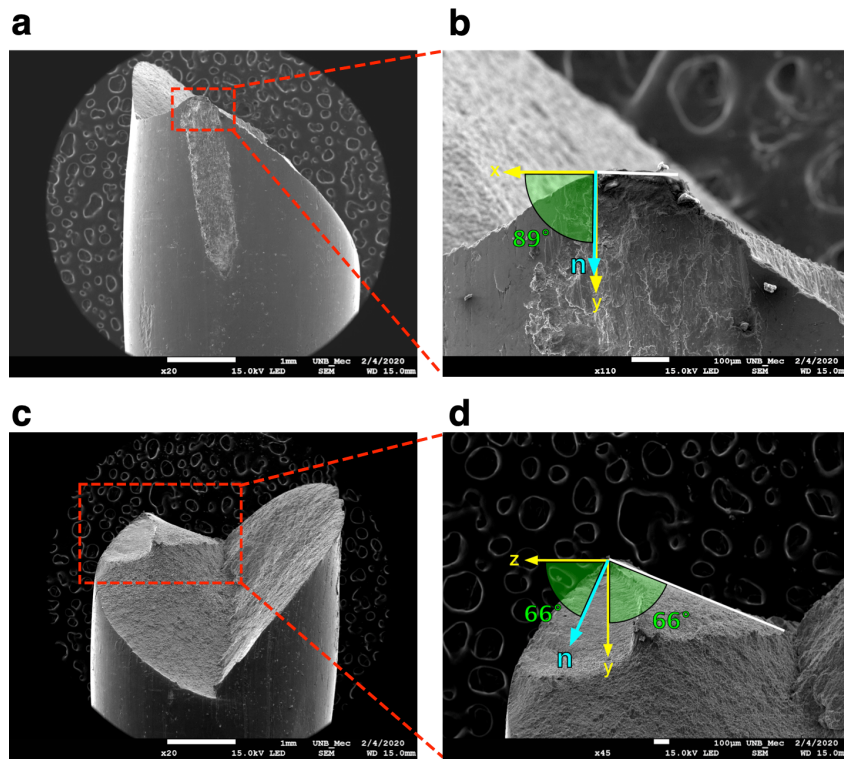




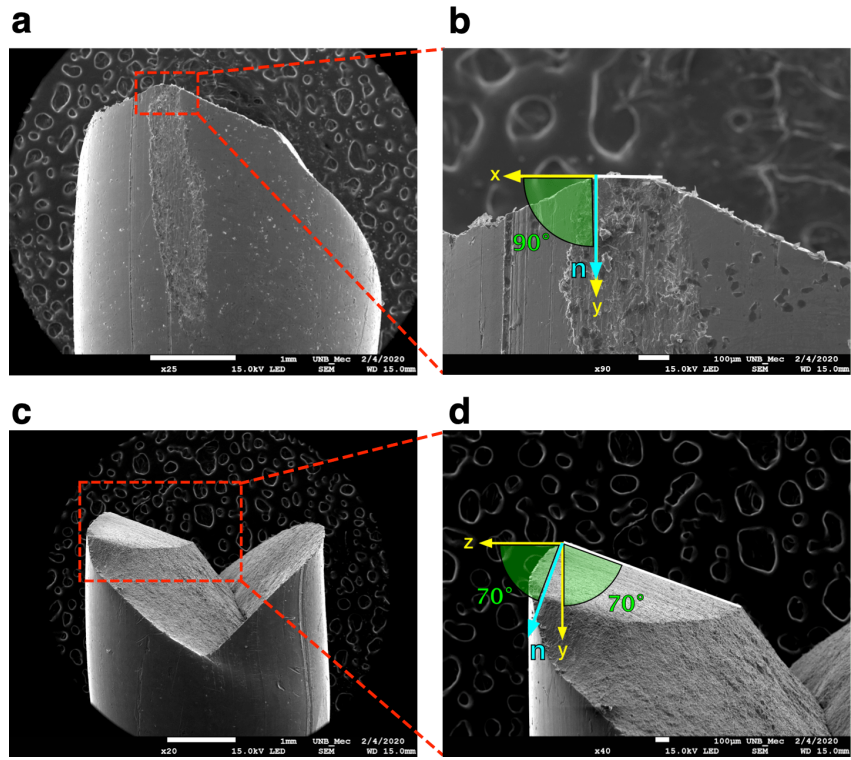
Specimen 08 ( $P = 500$  N,  $F_m = 2990$  N,  $N_f = 1,350,201$  cycles)



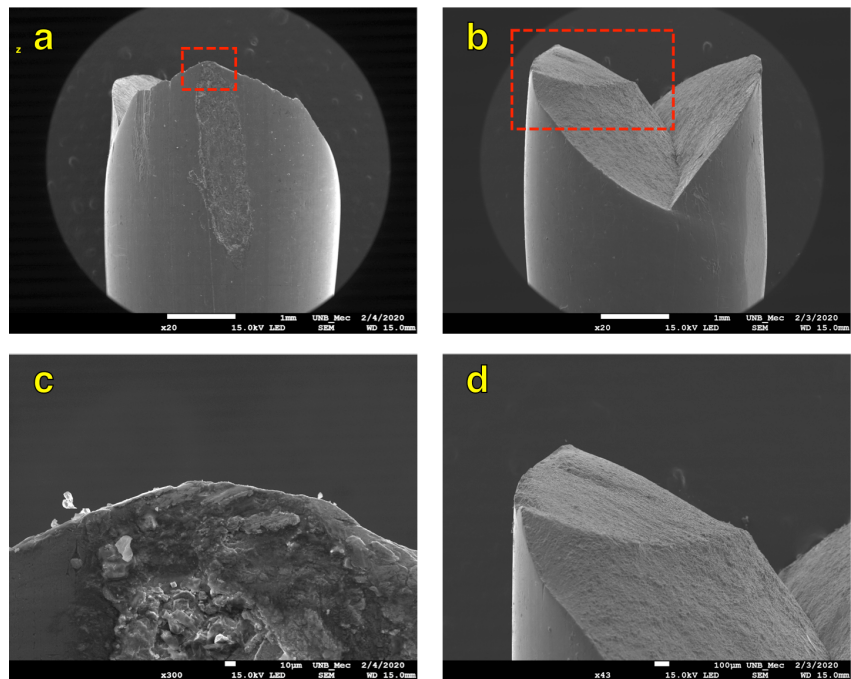
Specimen 24 ( $P = 500$  N,  $F_m = 2990$  N,  $N_f = 1,572,473$  cycles)



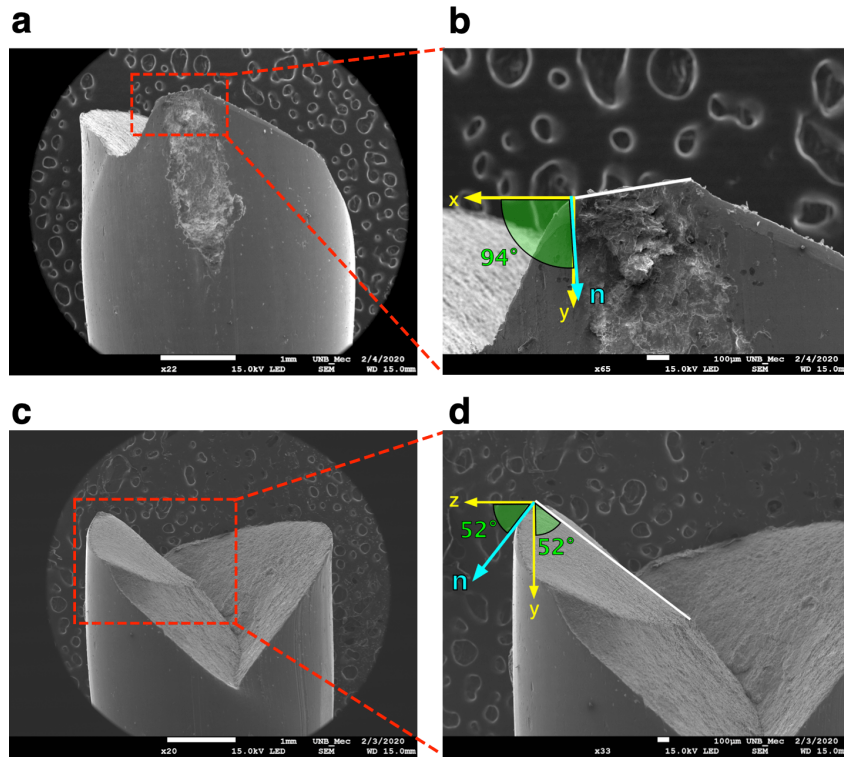
Specimen 23 ( $P = 500 \text{ N}$ ,  $F_m = 2800 \text{ N}$ ,  $N_f = 730, 520 \text{ cycles}$ )



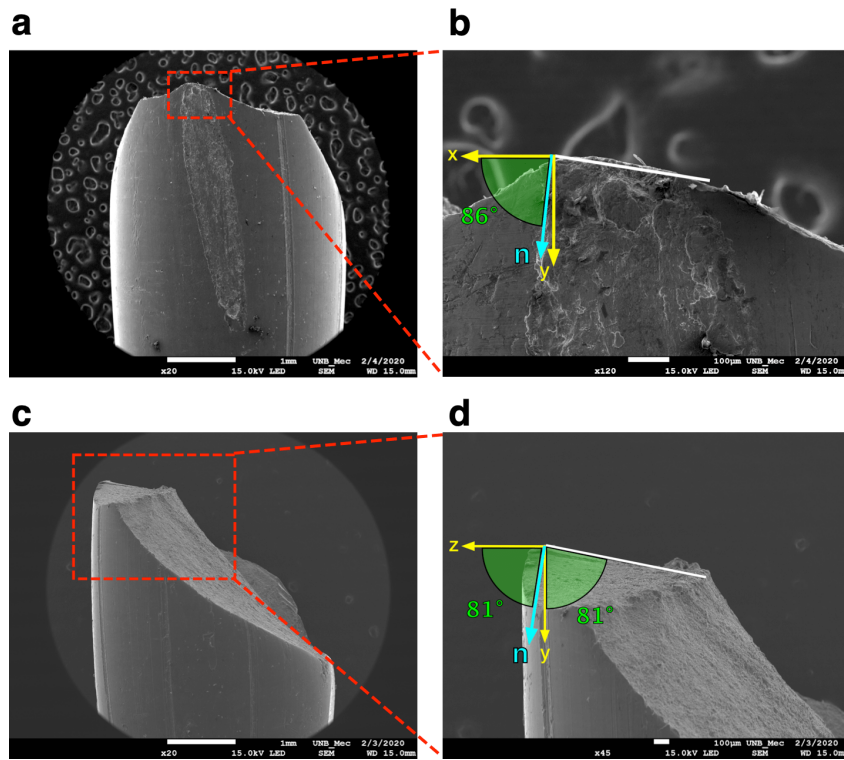
Specimen 02 ( $P = 500 \text{ N}$ ,  $F_m = 2800 \text{ N}$ ,  $N_f = 2, 844, 101 \text{ cycles}$ )



Specimen 11 ( $P = 500 \text{ N}$ ,  $F_m = 2600 \text{ N}$ ,  $N_f = 853,072 \text{ cycles}$ )

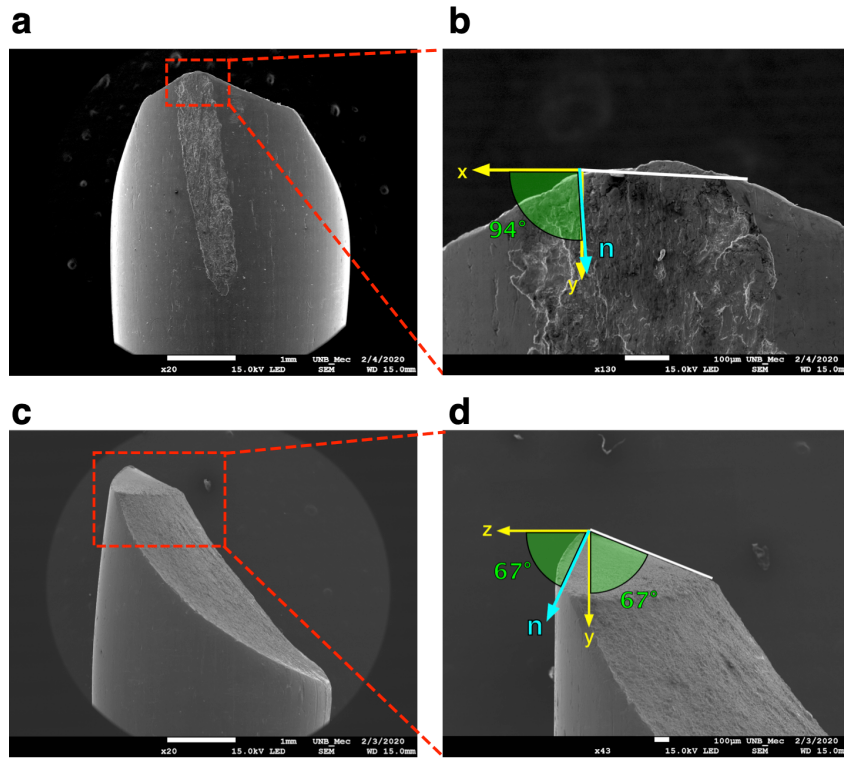


Specimen 17 ( $P = 750 \text{ N}$ ,  $F_m = 3150 \text{ N}$ ,  $N_f = 4,610,117 \text{ cycles}$ )

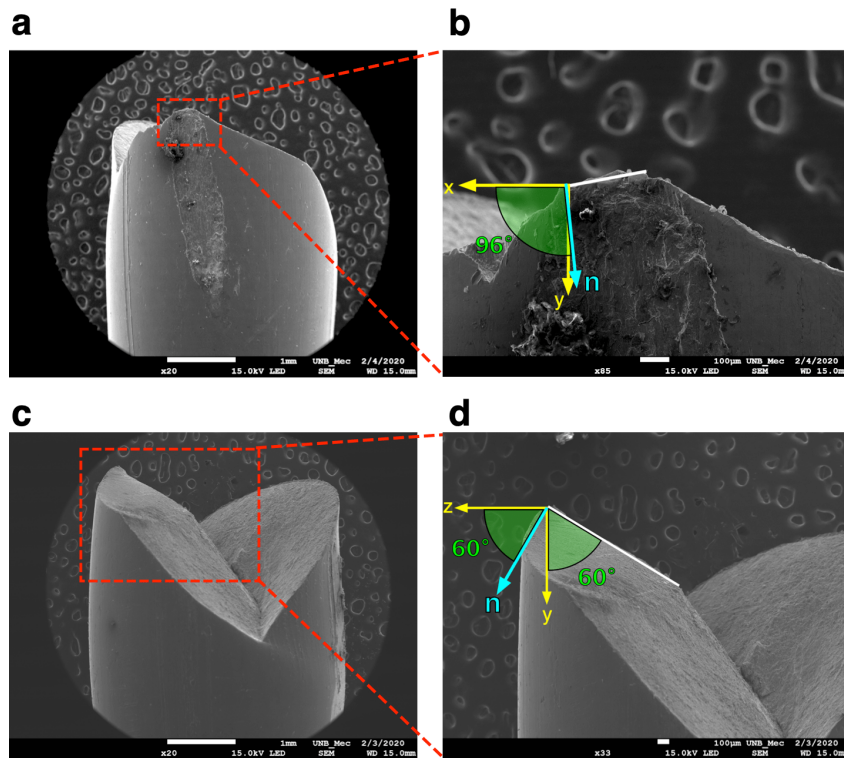




Specimen 06 ( $P = 750 \text{ N}$ ,  $F_m = 3150 \text{ N}$ ,  $N_f = 4,773,894 \text{ cycles}$ )


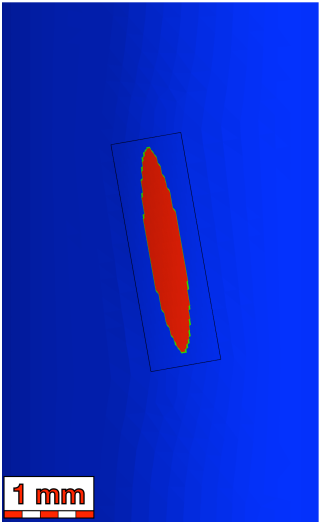

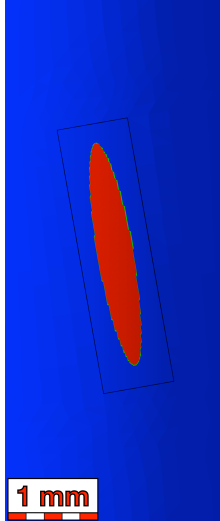


Specimen 10 ( $P = 750 \text{ N}$ ,  $F_m = 2800 \text{ N}$ ,  $N_f = 4,640,891 \text{ cycles}$ )




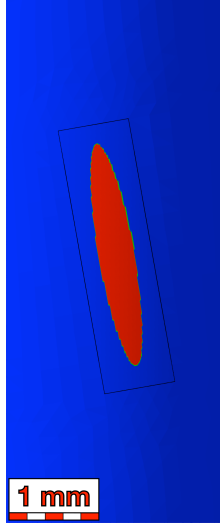
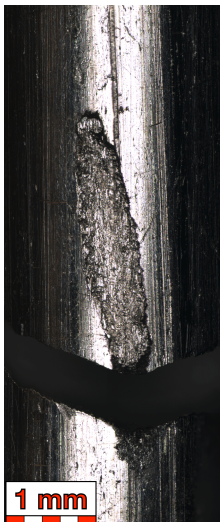
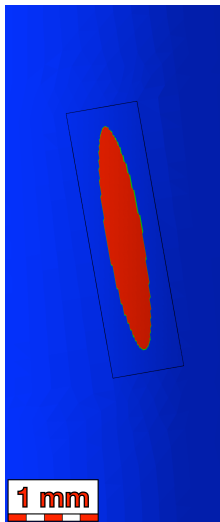


## C Observed and estimated contact marks

Specimen ID	$P$ [N]	$F_m$ [N]	Observed Mark	Estimated Mark
01	500	3150	 A grayscale photograph of a contact mark on a metal surface. The mark is a dark, elongated, and somewhat irregular shape. A 1 mm scale bar is visible at the bottom left of the image.	 A blue background with a red, elongated, oval-shaped area representing the estimated contact mark. A black rectangular box outlines the red area. A 1 mm scale bar is visible at the bottom left of the image.
08	500	2990	 A grayscale photograph of a contact mark on a metal surface. The mark is a dark, elongated, and somewhat irregular shape. A 1 mm scale bar is visible at the bottom left of the image.	 A blue background with a red, elongated, oval-shaped area representing the estimated contact mark. A black rectangular box outlines the red area. A 1 mm scale bar is visible at the bottom left of the image.

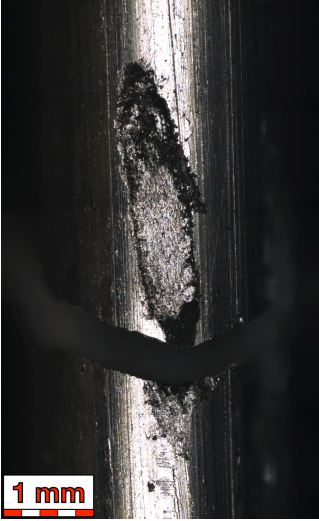
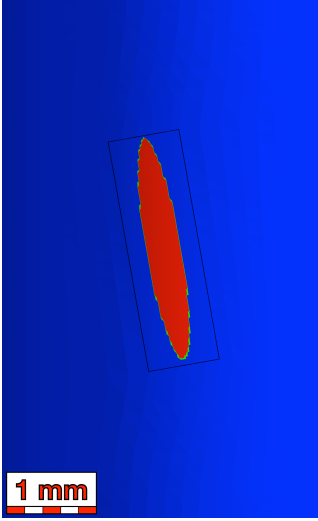

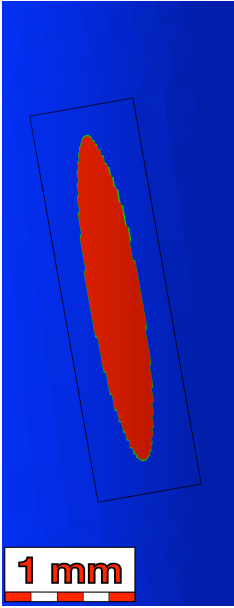
*(continued on next page)*

Table C.1, continued

Specimen ID	$P$ [N]	$F_m$ [N]	Observed Mark	Estimated Mark
24	500	2990		
23	500	2800		


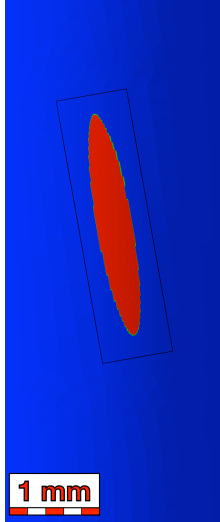

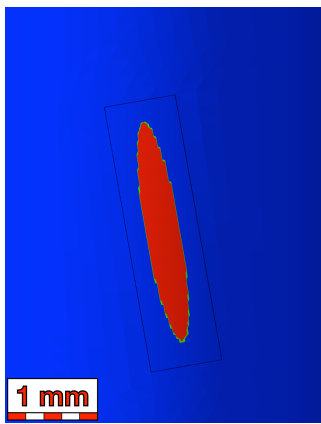

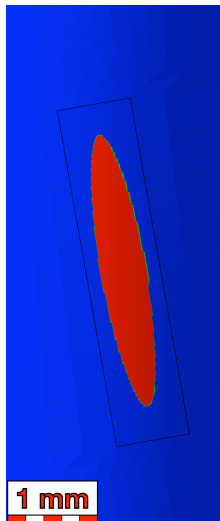
(continued on next page)

Table C.1, continued

Specimen ID	$P$ [N]	$F_m$ [N]	Observed Mark	Estimated Mark
02	500	2800		
11	500	2600		


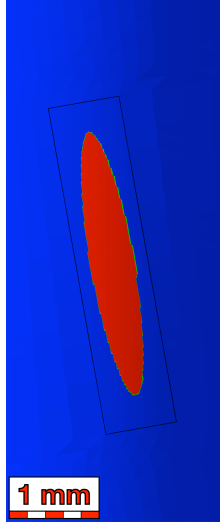
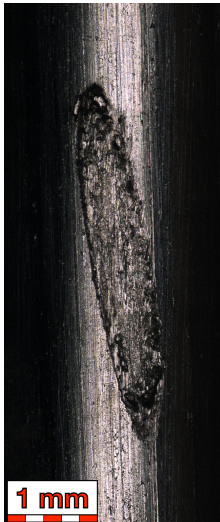
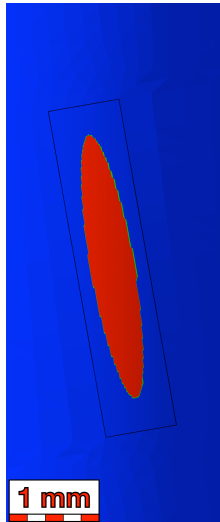
(continued on next page)

Table C.1, continued

Specimen ID	$P$ [N]	$F_m$ [N]	Observed Mark	Estimated Mark
25	500	2600		
04	500	2490		
17	750	3150		

(continued on next page)

Table C.1, continued

Specimen ID	$P$ [N]	$F_m$ [N]	Observed Mark	Estimated Mark
06	750	3150		
18	750	2990		

(continued on next page)

Table C.1, continued

Specimen ID	$P$ [N]	$F_m$ [N]	Observed Mark	Estimated Mark
10	750	2800	